Structure and Magnetism of Iron- and Chromium-Intercalated Niobium and Tantalum Disulfides

Lilia S. Xie,[†] Samra Husremovic,[†,¶] Oscar Gonzalez,[†,¶] Isaac M. Craig,[†,¶] and D. Kwabena Bediako[*,†,‡]

[†]*Department of Chemistry, University of California, Berkeley, California 97420, United States*

[‡]*Chemical Sciences Division, Lawrence Berkeley National Laboratory, Berkeley, California 94720, United States*

[¶]*Contributed equally to this work*

E-mail: bediako@berkeley.edu

Abstract

Transition metal dichalcogenides (TMDs) intercalated with spin-bearing transition metal centers are a diverse class of magnetic materials where the spin density and ordering behavior can be varied by the choice of host lattice, intercalant identity, level of intercalation, and intercalant disorder. Each of these degrees of freedom alters the interplay between several key magnetic interactions to produce disparate collective electronic and magnetic phases. The array of magnetic and electronic behavior typified by these systems renders them distinctive platforms for realizing tunable magnetism in solid-state materials and promising candidates for spin-based electronic devices. This Perspective provides an overview of the rich magnetism displayed by transition metal-intercalated TMDs by considering Fe- and Cr-intercalated NbS_2 and TaS_2. These four

exemplars of this large family of materials exhibit a wide range of magnetic properties, including sharp switching of magnetic states, current-driven magnetic switching, and chiral spin textures. An understanding of the fundamental origins of the resultant magnetic/electronic phases in these materials is discussed in the context of composition, bonding, electronic structure, and magnetic anisotropy in each case study.

Introduction

Transition metal dichalcogenides (TMDs) are a class of materials in which transition metals coordinated by bridging chalcogenides form two-dimensional layers that stack via van der Waals (vdW) interactions along the crystallographic c axis. This lamellar structure permits a range of different species to be intercalated into these vdW interfaces, including transition metals.[1–4] In these cases, intercalation can be considered as thermodynamically driven by a charge transfer reaction, in which electrons are transferred from the intercalating species to the conduction band of the host material. The resulting solid consists of positively charged intercalants embedded into an electron-doped host lattice.[5–7] For open-shell intercalants, local magnetic moments can be introduced into the lattice, giving rise to long-range magnetic order.[8,9] The diversity of possible intercalants and host lattices has long attracted attention to this class of materials as tunable platforms for studying the interplay among composition, structure, and magnetism. More recently, variation in the nature of defects and domain structures in these intercalated compounds have been appreciated as key factors that affect the exchange interactions and magnetic correlations,[10–13] resulting in complex magnetic phase spaces.

Among known magnetic intercalated TMDs, Fe- and Cr-intercalated NbS_2 and TaS_2 materials exhibit a wide range of behaviors depending on the intercalant's identity and stoichiometry. Their properties, which include sharp switching of magnetization,[14,15] low-current electrical switching of antiferromagnetic states,[13,16] and chiral spin textures,[17–19] have positioned these materials as potential candidates for spin-based electronic technologies (spin-

tronics). From a fundamental perspective, these exotic magnetic phases have also motivated detailed investigations into the many-body physics underlying their behavior, and the correlations between the compositions and magnetic properties of these systems have made them attractive platforms to study structure–property relationships in solid-state materials.

This Perspective aims to provide an overview of the magnetic properties of Fe- and Cr-intercalated NbS_2 and TaS_2, and to draw connections between magnetic order and fundamental differences in the electronic structure, which may guide future work on these systems. For example, significant differences in the properties of the Fe- and Cr-intercalated systems can be traced to stronger spin–orbit coupling (SOC) in the Fe-intercalated compounds from the unquenched orbital angular momentum of the Fe^{2+} centers. Consequently, the magnetic anisotropy in the Fe-intercalated TMDs is substantially different from the Cr-intercalated analogues: the c axis is the easy axis of magnetization in the Fe-based derivatives, while it is the hard axis in the Cr-based compounds. Other factors, such as disparate magnitudes of SOC from the NbS_2 and TaS_2 host lattices, result in further distinctions in each of the intercalated compounds.

To provide a background for understanding their magnetic behavior, a primer is provided on the basic electronic structure, intercalant superlattices, and magnetic exchange interactions in these materials. Subsequently, notable magnetic properties are presented for the four materials that constitute the focus of this Perspective, Fe_xTaS_2, Fe_xNbS_2, Cr_xNbS_2, and Cr_xTaS_2. Fe_xTaS_2 exhibits either ferromagnetic (FM) or antiferromagnetic (AFM) ordering at different intercalation levels.[12,14,20–22] Fe_xNbS_2 exhibits spin glass behavior that has been shown to coexist with and couple to local AFM domains, leading to many unconventional and technologically relevant properties.[13,16,23,24] Cr_xNbS_2 and Cr_xTaS_2 both exhibit chiral spin textures when $x = 1/3$, with different concentrations of topologically-protected magnetic solitons that evolve with field and temperature.[17–19,25,26] Key experimental findings for this family of materials are summarized, and future directions and open questions are discussed.

Intercalation into NbS_2 and TaS_2

Like many TMDs, NbS_2 and TaS_2 occur in several different polytypes, in which the coordination of the transition metal can be either trigonal prismatic (D_{3h}) or octahedral (O_h).[5] The $2H$ polytype of these materials, in which all the metal centers have D_{3h} coordination, is the most widely studied with respect to intercalation, and the scope of this Perspective will be limited to the materials with this structure. The $2H$ designation refers to the two layers in each hexagonal unit cell of this polytype, which crystallizes in the $P6_3/mmc$ space group.

Although the $2H$ polytype contains both octahedral and tetrahedral interstitial sites in the vdW interface (Figure 1), the experimentally determined crystal structures of Fe- and Cr-intercalated NbS_2 and TaS_2 compounds show intercalants occupying the octahedral sites exclusively.[1,2] This preference may be attributed to the geometry of the octahedral sites presenting the more favorable coordination environment and requiring minimal structural reorganization for first-row transition metal intercalants. However, transition metal intercalants are not limited to octahedral sites: for example, ZrS_2-based compounds contain intercalants in both tetrahedral and octahedral sites,[27] and Cu^+ intercalates into tetrahedral sites in NbS_2.[28] Additionally, intercalation or variations in stoichiometry may alter stacking arrangements or the availability of coordination sites: for example, non-stoichiometric NbS_2 and TaS_2 can contain Nb or Ta interstitials in the vdW interface.[29,30]

While Fe_xMS_2 and Cr_xMS_2 can be prepared from a solid-state reaction between the unintercalated host material and the elemental intercalant,[21] these compounds are more commonly synthesized from the constituent elements.[14,17] Disparate synthetic routes notwithstanding, to examine the thermodynamic feasibility for formation of the intercalation compound, we can consider the compounds Fe_xMS_2 and Cr_xMS_2 as products of a reaction between the MS_2 parent compound and the elemental intercalant species, as suggested by DiSalvo.[6] Within this framework, electrons are transferred from the neutral, zero-valent intercalant to the host material, generating oxidized, cationic intercalants and reduced (electron-doped) host lattice layers.

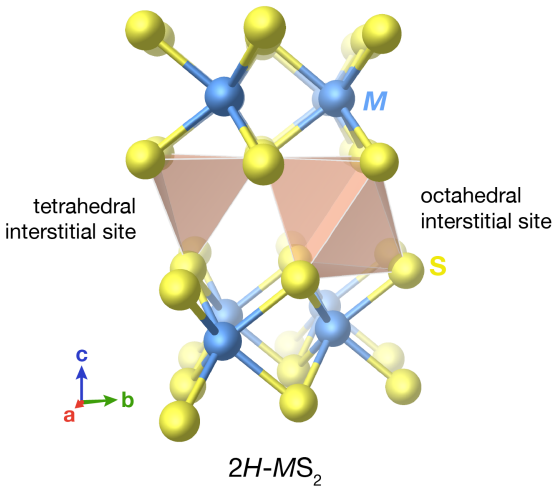

Figure 1: Intercalants can occupy tetrahedral (left) and octahedral (right) interstitial sites in the native structures of 2H TMDs.

This charge transfer can be rationalized phenomenologically by considering the work function of the intercalant and the electron affinity of the host material. In light of different conventions adopted in the physics and chemistry communities, in this Perspective, we define the work function as the minimum energy required to remove an electron from the solid into vacuum, and we define the electron affinity as the energy required to move an electron from the lowest unoccupied state of the conduction band to vacuum. Specifically, if the work function of the intercalant is less than the electron affinity of the host lattice, then one can expect that it will be energetically favorable for electrons from the intercalant to be transferred to the host lattice. The electron affinities for NbS_2 and TaS_2 are estimated to be 4.9 eV[31] and 4.8 eV,[6] respectively, and the work functions of Cr and Fe are 4.5 eV and 4.67 eV, respectively.[32] Consequently, we can anticipate energetically favorable electron transfer from the conduction bands of Cr and Fe to the conduction bands of NbS_2 and TaS_2 upon intercalation.

Electronic Structure

The metallic character of the NbS_2 and TaS_2 host materials can be rationalized through a simple electron counting scheme.[33] Formally, we expect the effective charge on the chalcogen centers to be -2, resulting in a $+4$ oxidation state for the transition metals and a d^1 electron configuration. Using crystal field theory as a first-order approximation, the trigonal prismatic coordination environment splits the Nb or Ta d orbitals into a_1' (d_{z^2}), e' ($d_{x^2-y^2}$, d_{xy}), and e'' (d_{xz}, d_{yz}) sets, in order of increasing energy. Therefore, one electron from Nb or Ta goes into a band with primarily d_{z^2} character, resulting in a partially filled band at the Fermi level (Figure 2, right side). The results of electron energy loss spectroscopy and photoelectron spectroscopy experiments[5,34] are consistent with this chemical intuition.

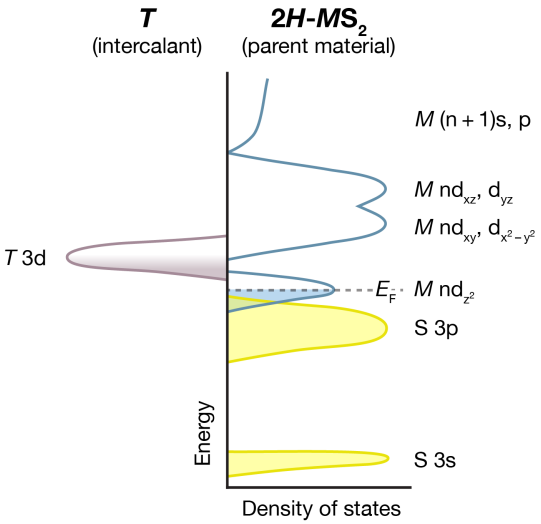

Figure 2: Qualitative representation of the density of states of (unintercalated) $2H$-NbS_2 or $2H$-TaS_2, with the majority parentage of states labeled. The Fermi level crosses the d_{z^2} band.

As discussed in the previous section, the intercalation compounds are, effectively, electron-doped derivatives of these parent compounds. For Cr or Fe as the intercalant, we can picture the partially filled $3d$ orbitals as lying higher in energy than the MS_2 d_{z^2} band, favoring electron transfer from the intercalant to the host lattice upon intercalation (Figure 2, left side), consistent with their relative work functions and electron affinities. This charge transfer may

therefore be envisioned as occurring from the Cr or Fe $3d$ bands to the host lattice conduction band of primarily d_{z^2} character. Experimentally, the intercalated compounds exhibit a higher filling level of the conduction band with primarily Nb or Ta d_{z^2} character compared to the unintercalated host materials.[35] These observations suggest that this rigid band approach is reasonable as a first approximation, and the extent of the band filling therefore depends on the oxidation state and stoichiometry of the intercalant in the host lattice.

Experimental magnetic susceptibility measurements on the intercalated compounds have shown that Cr is in the +3 oxidation state and Fe is in the +2 oxidation state.[8] In both cases, the coordination environment is a trigonally distorted pseudo-octahedron, which results in a qualitative d-orbital splitting diagram of e_g (d_{xy}, $d_{x^2-y^2}$), a_{1g} (d_{z^2}), and e_g (d_{xz}, d_{yz}). These charge states and the relatively weak crystal field result in a high-spin d^3 electron configuration for Cr^{3+} ($S = 3/2$), and a high-spin d^6 electron configuration for Fe^{2+} ($S = 2$).

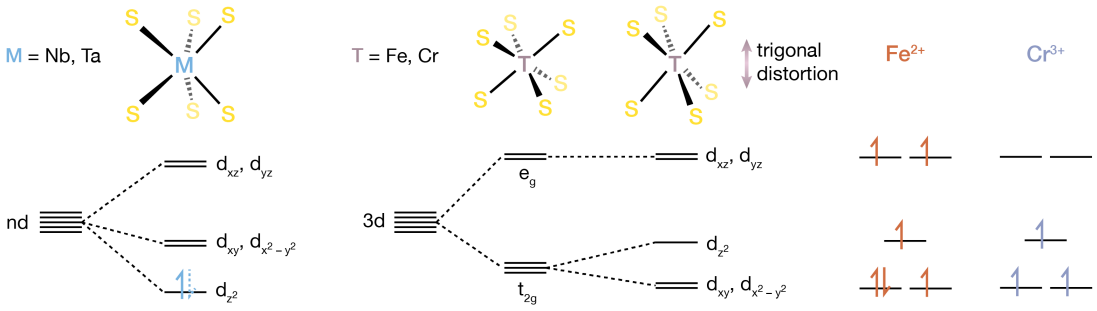

Figure 3: Qualitative d orbital splitting diagrams for the metal centers in $2H$-MS_2, M = Nb or Ta, and intercalants T = high-spin Fe^{2+} or Cr^{3+} in a trigonally distorted pseudo-octahedral coordination environment. The dashed electron in the M d_{z^2} orbital indicates that this state is more than half-filled after intercalation and the resulting electron transfer from the intercalant T to the MS_2 host lattice.

The Cr- and Fe-intercalated NbS_2 and TaS_2 materials studied to date are metallic, with general similarities in their electronic structures. However, the magnetic properties of each T_xMS_2 exhibit qualitative distinctions that can be understood to originate in part from the different electron configurations of the Cr and Fe intercalants. Specifically, in the case of Cr^{3+}, the orbital angular momentum is effectively quenched due to equal occupation of the e_g set of orbitals. SOC from the Cr center is thus small. In contrast, Fe^{2+} has an unevenly

occupied e_g set, leading to unquenched orbital angular momentum and larger SOC. This is essentially why the Cr compounds are soft ferromagnets,[17,25] while the Fe compounds are hard ferromagnets with high coercive fields.[14,22]

While these simple local ligand field models are useful as first approximations, the actual band structures of these compounds, according to experimental angle-resolved photoemission spectroscopy (ARPES) measurements and theoretical calculations, are necessarily more complicated.[25,36,37] Indeed, many important aspects of the magnetic behavior of these compounds—such as the c axis being the easy axis of magnetization in the Fe-intercalated materials, while it is the hard axis in the Cr-intercalated materials—cannot be explained without more thorough investigations of the spin-polarized band structures.[37] In later sections, we describe the results of experimental and computational studies into the electronic structure of each material in more detail.

Superlattice Structures

Crystallographic superlattices are observed at certain compositions of intercalated TMDs with the formula T_xMS_2, formed by periodic ordering of the intercalants into octahedral interstitial sites. Specifically, for Cr_xMS_2 and Fe_xMS_2 when M = Nb or Ta, perfect superlattices form, in principle, with $x = 1/4$ and $x = 1/3$. Taking $2H$-MS_2 with a lattice constant a_0, a supercell with $a' = 2a_0$ results when $x = 1/4$. In this case, the a and b axes of the supercell are coincident with the original axes of the parent TMD, and the space group of the parent TMD, $P6_3/mmc$, is retained. When $x = 1/3$, a supercell with $a' = \sqrt{3}a_0$ is formed, with the a and b axes rotated by 30° relative to the original axes. Unlike the parent TMD and the $2a_0 \times 2a_0$ (denoted 2×2 for short) superlattice, the $\sqrt{3}a_0 \times \sqrt{3}a_0$ (denoted $\sqrt{3} \times \sqrt{3}$ for short) superlattice is noncentrosymmetric, with space group $P6_322$.

Different views of the structures of the unintercalated parent TMD $2H$-MS_2 and the 2×2 and $\sqrt{3} \times \sqrt{3}$ T_xMS_2 superlattices are shown in Figure 4. When viewed along the c

crystallographic axis, intercalants in adjacent layers align in the 2×2 superlattice, whereas they do not align in the $\sqrt{3} \times \sqrt{3}$ superlattice (Figure 4b and c). When viewed along the a crystallographic axis, intercalants in the 2×2 superlattice line up in adjacent slabs (Figure 4d), whereas the intercalants in the $\sqrt{3} \times \sqrt{3}$ superlattice do not (Figure 4e). (These slabs are defined as cuts of the $(10\bar{1}0)$ plane for the 2×2 superlattice, and cuts of the $(2\bar{1}\bar{1}0)$ plane in the $[10\bar{1}0]$ direction for the $\sqrt{3} \times \sqrt{3}$ superlattice.)

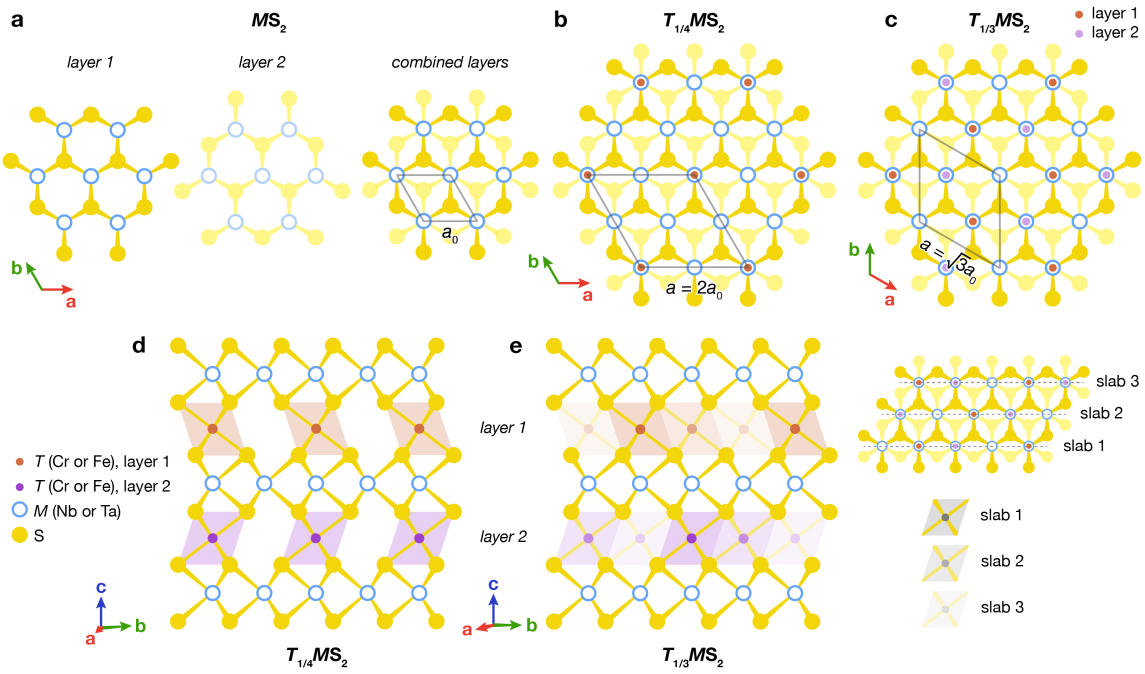

Figure 4: (a–c) Illustrations of the structures of two layers of an unintercalated $2H$-MS_2 parent TMD with lattice constant a_0; $T_{1/4}MS_2$ with an $a' = 2a_0$ supercell; and $T_{1/3}MS_2$ with an $a' = \sqrt{3}a_0$ supercell, all viewed along the c crystallographic axis. (d–e) Illustrations of the structures of $T_{1/4}MS_2$ and $T_{1/3}MS_2$ viewed parallel to the c crystallographic axis along $[2\bar{1}\bar{1}0]$ and $[10\bar{1}0]$, respectively. The slabs in (e) are defined as cuts of the $(2\bar{1}\bar{1}0)$ plane in the $[10\bar{1}0]$ direction, indicated on the right.

In addition to the different electron filling levels implied by their different compositions, the centrosymmetric nature of the 2×2 superlattice and noncentrosymmetric nature of the $\sqrt{3} \times \sqrt{3}$ superlattice is one of the most important distinctions between these structures. The absence of inversion symmetry profoundly affects the magnetic properties of materials T_xMS_2 with $x \sim 1/3$. Specifically, as we will discuss in more detail in later sections, the

Dzyaloshinskii–Moriya (DM) interaction arises from the lack of inversion symmetry in the $\sqrt{3} \times \sqrt{3}$ superlattice, resulting in spin canting and chiral magnetic ground states.[37]

Importantly, the illustrations shown in Figure 4 depict the ideal superlattices anticipated at the precise stoichiometries of $x = 1/4$ and $x = 1/3$ in these intercalated TMDs. However, experimental evidence of superlattice structures is present in many Fe_xMS_2 and Cr_xMS_2 compounds at different values of x. In these cases, defective superlattices are expected, possessing either missing intercalants or extra interstitial defects depending on whether x is less than or greater than the "precise" values of 1/4 or 1/3. Locally ordered/disordered domains can co-exist in these off-stoichiometry compounds, with interactions between these domains leading to bulk magnetic behavior that is distinct from the perfect superlattice. For instance, giant magnetoresistance is observed in $Fe_{0.28}TaS_2$,[11] and the coexistence of AFM and spin glass order leads to exchange bias in Fe_xNbS_2 for stoichiometries above and below $x = 1/3$.[13]

Origins of Magnetic Behavior

The nature of exchange interactions between unpaired electrons in a material determines the nature of long-range magnetic ordering. Among the types of exchange interactions that can be operative in solid-state materials are Heisenberg interactions, such as direct exchange and superexchange, and the Ruderman–Kittel–Kasuya–Yosida (RKKY) interaction.[38,39] Additional terms, such as the DM interaction and the magnetocrystalline anisotropy energy (MCAE), arise from both spin–orbit coupling and the underlying symmetry of the compound.[40,41] In this section, we introduce the terms thought to be most relevant to magnetic ordering in Fe- and Cr-intercalated NbS_2 and TaS_2, namely the RKKY interaction, the DM interaction, and MCAE. Excellent general introductions to magnetism in extended solids can be found elsewhere.[38,39,42–44]

Due to the distances and bonding motifs between intercalants in the Fe_xMS_2 and Cr_xMS_2

materials, direct exchange and superexchange are not expected to contribute to magnetic ordering. Instead, the RKKY interaction is usually considered as the dominant exchange interaction driving magnetic ordering.[8,9,36,40] The RKKY interaction, which is akin to the extended solid analogue of double exchange, refers to coupling of localized spin moments through conduction electrons. The exchange coupling $J_{ij}(r)$ is described by the relation[45–47]

$$J_{ij}(r) \propto sin\left(\frac{(\vec{k}_F^{\uparrow} + \vec{k}_F^{\downarrow}) \cdot \vec{R}_{ij}}{R_{ij}^3}\right) \tag{1}$$

in which k_F is the Fermi wave vector corresponding to the spin of the conduction charge carrier, and R_{ij} is the distance between two magnetic centers i and j. According to Equation 1, the coupling J_{ij} oscillates between FM ($J_{ij} < 0$) and AFM ($J_{ij} > 0$) with varying R_{ij}. In other words, the distance between spin-bearing centers determines the nature of the exchange interaction. The RKKY formalism was first devised to describe coupling between nuclear spins,[45] and was later leveraged to describe coupling between localized moments from unpaired d and f electrons assuming minimal hybridization with the conduction band.[46,47] Because the the Fe_xMS_2 and Cr_xMS_2 materials are metallic, it is thought that the localized Fe or Cr $3d$ electrons couple through the delocalized electrons in the conduction band with predominantly Nb $4d_{z^2}$ or Ta $5d_{z^2}$ character. However, we note that some evidence suggests the magnetic properties of these compounds are affected by their electronic structure in more complex ways than explained by the second-order perturbation of RKKY theory.[25,48]

The DM interaction (also known as antisymmetric exchange) arises from SOC and broken inversion symmetry of the lattice.[40,49–51] The interaction takes the form $-\sum_{i\neq j} \vec{D}_{ij} \cdot (\hat{S}_i \times \hat{S}_j)$, in which $\vec{D}_{ij}$ is a DM vector between neighboring intercalants i and j. In noncentrosymmetric systems, such as $T_{1/3}MS_2$ with a $\sqrt{3} \times \sqrt{3}$ superlattice structure, DM interactions favor canting between neighboring spins and can result in chiral spin textures.[52] For instance, the $Cr_{1/3}MS_2$ materials exhibit chiral helimagnetic ground states,[17–19,26] and spin canting has been proposed in $Fe_{1/3}NbS_2$.[24] In Figure 5, the geometry of the DM interaction in a generic $T_{1/3}MS_2$ compound with a $\sqrt{3} \times \sqrt{3}$ superlattice is illustrated. The overall DM

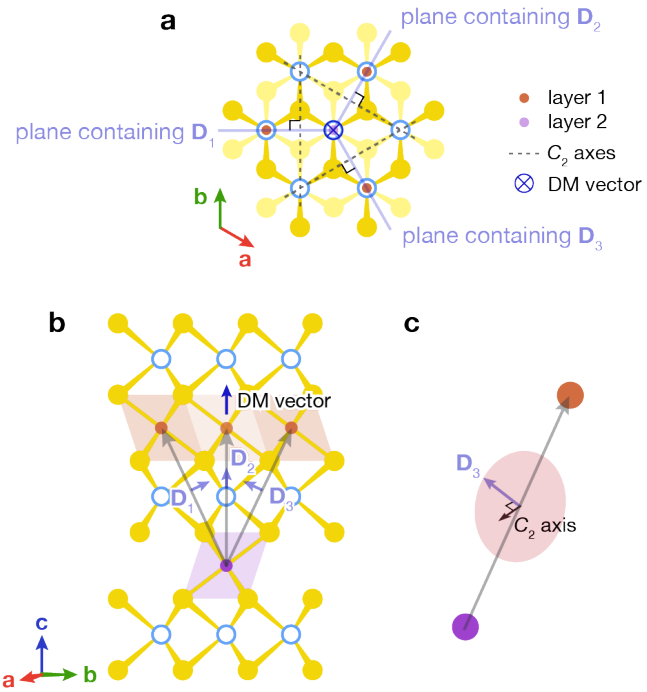

Figure 5: Dzyaloshinskii–Moriya interactions following Moriya's rules in $T_{1/3}MS_2$ systems with $P6_322$ symmetry. (a) View down the c–axis of $T_{1/3}MS_2$ that shows the planes containing the DM vectors along with the C_2 axes to show adaptation of Moriya's rules. (b) View of $T_{1/3}MS_2$ along the $[10\bar{1}0]$ direction where the gray arrows represent the coupling between one Cr atom (bottom, purple) with the three nearest Cr atoms in the adjacent layer (orange, top). (c) Demonstrates that the DM vectors, in this case $\vec{D}_3$, lie on a circle that is perpendicular to the C_2 axis.

vector $\vec{D}$ is the sum of the individual DM vectors $\vec{D}_1$, $\vec{D}_2$, and $\vec{D}_3$ derived using Moriya's rules[50] between interlayer nearest-neighbor intercalants. The resulting $\vec{D}$ lies parallel to the c axis, hence favoring the alignment of spins perpendicular to c. This effect is more evident in the $Cr_{1/3}MS_2$ systems, where competition between the DM and Heisenberg (FM) interactions causes spins in adjacent layers to align perpendicular to c with a characteristic angle between their orientations. These spin textures are discussed further in later sections of this Perspective.[19,40]

The MCAE is a special case of magnetic anisotropy that arises from SOC and is related to the crystal structure of a magnetic material.[39] Because of the lattice crystal field's inherent anisotropy, spins align preferentially along specific crystallographic directions, which are called the easy axes (or planes) of magnetization. Disparate orbital magnetic moments from Fe and Cr result in an easy axis along c in Fe_xMS_2, and an easy plane perpendicular to c in Cr_xMS_2.[37]

Iron-Intercalated Niobium and Tantalum Sulfides

Although Fe_xTaS_2 and Fe_xNbS_2 are isostructural and isoelectronic, they exhibit distinct magnetic ground states: for $x < 0.4$, Fe_xTaS_2 orders ferromagnetically while Fe_xNbS_2 orders antiferromagnetically, with easy axes along c. Their magnetic properties are sensitive to small changes in composition, especially around the commensurate superlattice stoichiometries of $x = 1/4$ and $x = 1/3$. Compounds with uniform 2×2 or $\sqrt{3} \times \sqrt{3}$ superlattices exhibit sharp magnetic transitions,[14,22,24,53] while off-stoichiometric Fe_xTaS_2 shows broadened magnetization switching and large magnetoresistance,[11,12] and Fe_xNbS_2 with $x \neq 1/3$ exhibits spin glass behavior and resistive switching.[13,24] Overall, studies on these materials indicate that interactions between ordered and disordered microscopic domains can dramatically affect their bulk properties. The precise origins of the dramatically different magnetic behavior of Fe_xTaS_2 and Fe_xNbS_2, and the role played by host lattice SOC, remains an open

question of interest.

Fe_xTaS_2

Fe_xTaS_2 exhibits diverse magnetic properties depending on the Fe intercalation level. The Fe stoichiometry affects the spacing between the spin-bearing intercalants, thereby altering their magnetic exchange interactions and spatial symmetry. AFM exchange interactions dominate for high intercalation amounts ($x > 0.4$),[21] while long-range FM ordering is observed in crystals with $0.2 \leq x \leq 0.4$.[12,20]

Within the FM intercalation regime, the Fe^{2+} ions are arranged in the 2×2 supercell for $0.2 \leq x \leq 0.26$, while the $\sqrt{3} \times \sqrt{3}$ superlattice is observed for $0.264 \leq x \leq 0.4$. When the Fe amount deviates from $x = 1/4$ and $1/3$, a commensurate superlattice with crystallographic defects (vacancies or interstitials) is formed.[10–12,20] Thus, the iron stoichiometry has profound effects on the crystallographic ordering of the intercalants. Nevertheless, the local coordination environments of the Fe^{2+} centers in these materials are equivalent (trigonally distorted pseudo-octahedral) (Figure 3).[36,54] The resulting unquenched orbital angular momentum contributes to a large magnetocrystalline anisotorpy energy (MCAE) across the Fe_xTaS_2 family.

This large MCAE makes it energetically costly to tilt the magnetization away from the most favorable direction (i.e. the easy axis) along the c axis.[11,14,15,36] For example, the saturation magnetization of $Fe_{0.25}TaS_2$ was reached with a field of 3.8 T applied parallel to c.[36] In contrast, the saturation field perpendicular to c was estimated to be 60 T due to the very weak response in this orientation.[36] Overall, the very favorable spin alignment along c, because of the large MCAE, plays an important role in shaping the magnetic properties of Fe_xTaS_2.[11,12,36]

Considering the large MCAE of Fe_xTaS_2, the differences in magnetic behavior with changes in Fe content are usually attributed to changes in the exchange interactions as x is modulated. The effect of Fe stoichiometry on magnetic properties is highlighted in

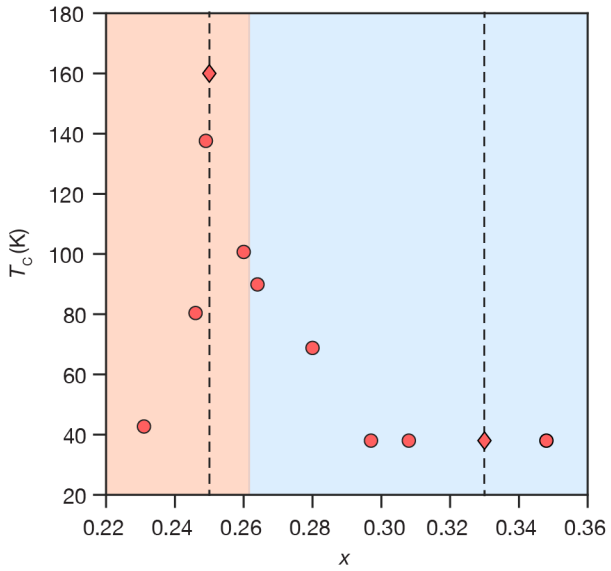

Figure 6: Dependence of T_C in Fe_xTaS_2 on the Fe intercalation amount (x). Data points corresponding to the commensurate superlattices are represented by diamond markers and marked with dashed lines, while other data points are represented by circles. The orange- and blue-shaded regions indicate the intercalant regimes in which the 2×2 and $\sqrt{3} \times \sqrt{3}$ superlattices are observed, respectively. The data were obtained from Hardy et al.[11], Chen et al.[12], Morosan et al.[14], Mangelsen et al.[22], Zhang et al.[55]

Figure 6, where the Curie temperature, T_C, is plotted for different values of x. T_C is highest ($\sim$160 K) for $Fe_{0.25}TaS_2$, and declines sharply as the stoichiometry diverges from this amount. Interestingly, the T_C reaches a plateau at 38 K around the commensurate $x = 0.33$ stoichiometry. This trend in T_C indicates that overall, the FM exchange interactions are strongest when the intercalants are arranged in the ordered 2×2 superlattice. Additionally, relatively small deviations ($\delta x \leq 0.03$) from $x = 0.25$ lead to crystallographic defects that ultimately weaken the uniformity of the exchange interactions and substantially lower the ordering temperature. In contrast, the overall FM exchange interactions for the $\sqrt{3} \times \sqrt{3}$ superlattice appear to be significantly weaker, and notably, small deviations ($\delta x \leq 0.03$) in intercalation levels do not appear to significantly affect the strength of magnetic exchange for this structure, based on unchanging T_C.

The substantial differences in magnetic behavior depicted in Figure 6 may arise from key differences in electronic structures of the two superlattice systems, which may engender *distinct types* of magnetic exchange interactions. The RKKY model, which is generally used to describe the magnetic exchange interactions for the Fe_xTaS_2 family, applies most rigorously in systems with *localized magnetic moments.*[38,45,48,56,57] Accordingly, the RKKY model could serve as a good description of magnetic exchange in Fe_xTaS_2 provided the electronic band structure of the host is not significantly altered by intercalation aside from charge transfer from the intercalants raising the Fermi level (rigid-band model).[58] However, strong hybridization of the Fe electronic states with conduction bands of the TaS_2 host lattice would give rise to a more itinerant magnetism of the conduction electrons[38] that would be less reliably described by RKKY exchange. Electronic band structure calculations,[36] ARPES,[36] and radio-frequency magnetic susceptibility[59] suggest that the rigid-band model and local moment ferromagnetism closely approximate the properties of $Fe_{0.25}TaS_2$. However, the high degree of hybridization between the Fe and Ta bands in $Fe_{0.33}TaS_2$ appears to render the rigid-band (RKKY) model inaccurate.[58,60] Fundamentally different mechanisms of magnetic exchange in $Fe_{0.25}TaS_2$ and $Fe_{0.33}TaS_2$ may therefore account for their substantial differences

in magnetic behavior.

Another possible explanation for the differences in magnetic exchange in Fe_xTaS_2 for x = 0.25 and 0.33 is the presence of some spin canting in the $\sqrt{3} \times \sqrt{3}$ superlattice. Even though deviation of spin alignment from the c axis would be unfavorable due to MCAE, some degree of canting away may be stabilized by: (1) DM interactions (Figure 5) arising from the breaking of inversion symmetry[61] in the $\sqrt{3} \times \sqrt{3}$ supercell, or (2) an AFM component in the magnetic exchange, which could emerge from differences in the carrier densities[15,22,61] and intercalant spacings for the $x = 0.33$ structure compared to the $x = 0.25$ system. Regardless of the origin, spins canting away from the out-of-plane FM order could decrease T_C,[12,62] potentially explaining differences in T_C across the phase diagram.

Even though additional studies into the electronic structures and magnetic exchange interactions of these materials are needed to clarify these trends, we can gain additional valuable insight into their physics through a detailed analysis of their magnetic and transport properties. In particular, an examination of the magnetic characteristics of Fe_xTaS_2 as a function of Fe stoichiometry reveals profound changes in coercivity, sharpness of magnetization switching, and magnetoresistance (Figure 7) as x is modulated. As examples, we consider the magnetic and transport characteristics of four Fe_xTaS_2 compounds with x = 0.25,[14] 0.28,[11] 0.33[22] and 0.348.[12]

Below T_C, intercalation compounds with the commensurate $x = 0.25$ and 0.33 Fe stoichiometries exhibit very sharp switching of magnetization (Figure 7). This behavior indicates that the magnetic exchange interactions in the commensurate supercells are highly uniform, such that all of the magnetic moments flip synchronously when a sufficiently large field is applied.[12] In contrast, the off-stoichiometric Fe_xTaS_2 crystals generally display magnetic hysteresis curves with broader switching (Figure 7), which is a direct result of magneto–structural disorder. In the vicinity of crystallographic defects (e.g. Fe vacancies or interstitial defects), perturbations to the magnetic coupling of neighboring intercalants produces weaker exchange coupling.[11,12] Consequently, as the external field is swept, these weakly

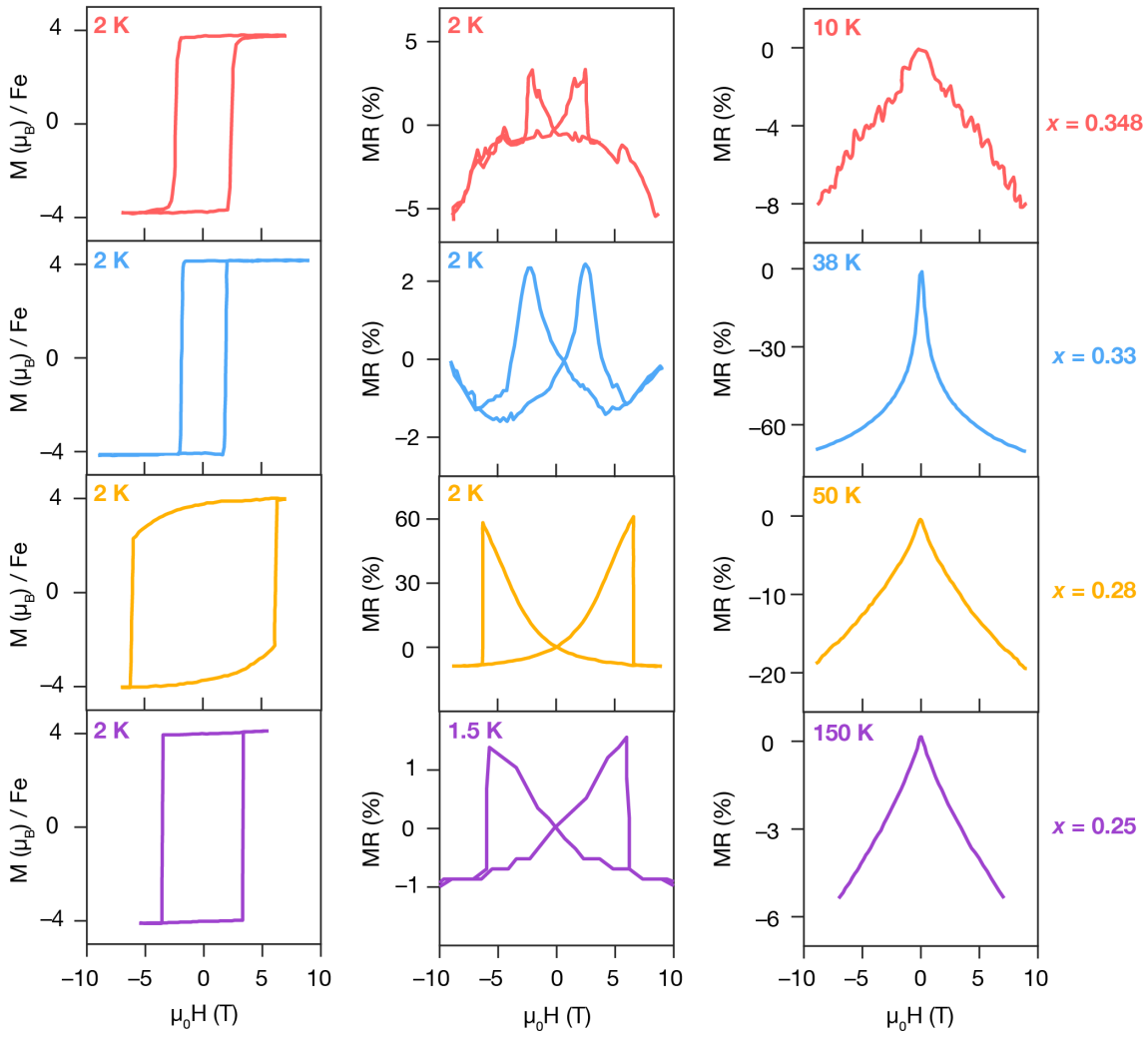

Figure 7: Magnetization at 2 K, MR (%) at $\leq$ 2 K and MR (%) at an elevated temperature below T_C for $Fe_{0.25}TaS_2$, $Fe_{0.28}TaS_2$, $Fe_{0.33}TaS_2$ and $Fe_{0.348}TaS_2$. All the data was obtained with the current in the *ab* plane and the field along the *c* axis. The data were digitized and replotted from Checkelsky et al.,[15] Hardy et al.,[11] Mangelsen et al.,[22] and Chen et al.,[12] respectively.

coupled moments are flipped first and become misaligned (antiparallel) to the bulk magnetization.[11,12] This asynchronous flipping of magnetic moments engenders broad M vs. H curves (Figure 7).[11] These magnetic hysteresis data also highlight that the coercive fields (H_C, the magnetic fields required to demagnetize the magnet below T_C), are strongly dependent on x. Although FM Fe_xTaS_2 compounds generally exhibit high H_C due to their large MCAE, variations in the magnetic exchange interactions and defect concentrations produce substantial differences in coercivity as x is varied. The H_C at 2 K for $Fe_{0.25}TaS_2$ is higher than that of $Fe_{0.33}TaS_2$, once again highlighting the differences in their magnetic exchange interactions despite both having commensurate superlattices (Figure 7). Interestingly, the off-stoichiometric samples have higher coercivities compared to the commensurate superlattices. This may seem counterintuitive, as their magnetic exchange interactions are less homogeneous, but defects in the disordered samples can pin magnetic domains and increase the coercivity.[12] This observation highlights the importance of characterizing structural disorder across the Fe_xTaS_2 family.

In addition to affecting the magnetization response, the intercalation level also strongly impacts the electronic transport properties of Fe_xTaS_2 materials. Misaligned magnetic moments in the off-stoichiometric Fe_xTaS_2 materials strongly scatter carrier electrons, leading to large magnetoresistance (MR) below T_C (Figure 7).[11,12] The MR increases with the proportion of misaligned spins, reaching a maximum value at H_C, the point with maximum spin disorder. With $H > H_C$, all spins align with the external field and the MR decreases, resulting in bow tie-shaped MR curves. The spin disorder-induced MR is largest for samples with $0.25 < x < 0.33$: the MR at 2 K for $x = 0.28$ reaches 60% (Figure 7), while the highest MR reported is 140% at 2.3 K for $x = 0.297$.[12] These MR values are comparable with industrially relevant giant magnetoresistance observed in magnetic multilayers.[63–65] Interestingly, for $x = 0.264$ (i.e. only 0.014 greater than 0.25), the MR (4 K) increases from $< 1\%$ to 35%.[12,14,15] However, for $x = 0.348$ (i.e. 0.015 greater than 0.33), the MR (2 K) only increases from $\sim 2\%$ to $\sim 4\%$ (Figure 7).[12,22] This discrepancy suggests that the $\sqrt{3} \times \sqrt{3}$ superlattice

retains relatively uniform magnetic exchange interactions with small amounts of structural disorder, or that spin–disorder scattering is relatively insensitive to inhomogeneities in this material. In summary, the composition of Fe_xTaS_2 materials generally influences their magnetic exchange interactions and determines the extent of spin-disorder scattering, presenting an avenue for fine-tuning MR response.

For both stoichiometric superlattices with $x = 0.25$ and 0.33, spin-disorder scattering appears to be absent, consistent with magneto-structural homogeneity in these systems.[12] For these commensurate materials, the MR at high field is minimal at low temperatures.[15,22] However, the MR response increases near T_C (Figure 7), reaching a maximum of -72% for $x = 0.33$.[22] This temperature-dependent behavior is characteristic of MR arising from field suppression of thermally activated collective spin excitations (magnons), which are most pronounced around T_C.[15,66,67] However, the precise origin of much higher MR at high temperatures for $Fe_{0.33}TaS_2$ compared to all other stoichiometries is yet to be elucidated.

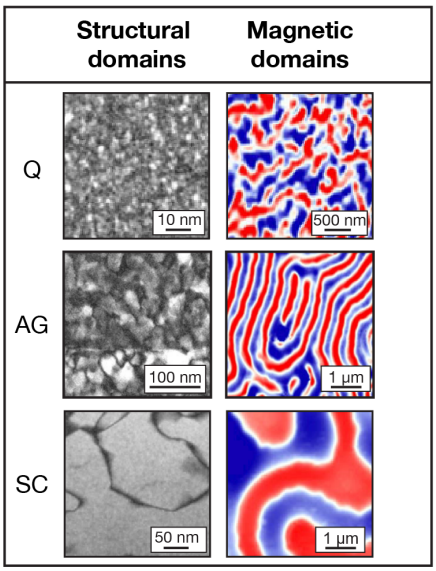

Figure 8: Structural domains of $Fe_{0.25}TaS_2$ were imaged using dark-field TEM by selecting the superlattice peaks for the quenched (Q), as-grown (AG) and the slowly cooled (SC) specimens. The magnetic domains of the same samples were imaged with magnetic force microscopy (MFM). Adapted with permission from Choi, Y. J.; Kim, S. B.; Asada, T.; Park, S.; Wu, W.; Horibe, Y.; Cheong, S.-W. *Europhys. Lett.* **2009**, *86*, 37012. Copyright 2009 IOP Publishing.[68]

Apart from stoichiometry, the thermal history during crystal growth can also modulate structural order/disorder in commensurate $Fe_{0.25}TaS_2$. This was demonstrated by Choi et al.,[68] who characterized the magneto-structural properties of three differently grown $Fe_{0.25}TaS_2$ specimens: as-grown (AG, compound was left to cool in the furnace after growth), slowly cooled (SC, cooled at 2 °C/hr from 700 °C), and quenched (Q, removed from 700 °C and soaked in ice water) (Figure 8). The H_C (2 K) values of these crystals differed considerably (2.7 T, 4 T and 7 T for the SC, AG and Q samples, respectively). Dark-field (DF) transmission electron microscopy (TEM) images revealed that crystallographic domain boundaries (dark contrast in Figure 8) are the most ubiquitous for the Q sample, while the SC sample has the lowest density of these domain boundaries. Magnetic force microsocpy (MFM) revealed that the size of the crystallographic and magnetic domains are correlated in these systems. These results highlight the influence of synthetic conditions on the ensemble magnetic properties of Fe_xTaS_2 via longer-range structural disorder and domain formation.

In conclusion, Fe_xTaS_2 compounds host a plethora of magnetic behaviors that are strongly influenced by structural order/disorder. Because their magneto-structural properties are tightly associated, crystallographic disorder engenders some of the most interesting characteristics of these materials, such as extremely high coercivities and giant magnetoresistance. However, the relationships between local disorder, magnetic exchange, and long-range magnetic order still require elucidation over a wider composition space of the diverse Fe_xTaS_2 family.

Fe_xNbS_2

While the material was first studied in the 1970s,[2,3,35] recent discovery of ultra-low current switching in Fe_xNbS_2 has prompted investigation into the origin of this behavior, as it occurs with much lower currents than other materials and displays unconventional behavior such as single-pulse saturation.[16] Unlike its Ta analogue, Fe_xNbS_2 forms an AFM phase at both $x = 1/4$ and $x = 1/3$, with the easy axis along the c axis and Néel temperatures of

approximately 145 K[23] and 45 K,[69] respectively. The triangular sublattice formed by the intercalants necessitates that an AFM ground state must be frustrated.[70,71] These frustrated AFM exchange interactions play a crucial role in the formation of a spin glass phase for off-stoichometric intercalation densities and set the complex magnetic phase space of this material. As both play a role in the proposed resistive switching mechanism, a detailed understanding of the magnetic order and its interplay with spin-glass order is crucial to understand the unconventional and technologically advantageous behavior of Fe_xNbS_2.

Spin glasses are of interest in part because they are the simplest realization of a glassy system, in which a low-temperature disordered phase displays characteristically slow dynamics. They have accordingly served as a platform to understand glassy behavior more generally, including the nature of its history-dependent response and its many possible ground states, including both metastable and stable equilibrium states.[72] Spin glasses often exhibit a characteristic cusp in magnetic susceptibility below the freezing temperature associated with the spin glass phase transition.[72,73] Below this freezing temperature, the field-cooled and zero-field-cooled magnetization curves diverge, because the applied field biases the sample into a given metastable state.[72,74,75] Spin glass systems also exhibit a slow relaxation from the field-cooled frozen state after the applied field is removed, indicative of glassy dynamics.[72,74,75]

In Fe_xNbS_2, the spin glass behavior is attributed to the presence of disordered interstitial Fe^{2+} ions or vacancies coupled via an oscillatory exchange mechanism (i.e. RKKY).[76,77] Because of variation in the distance between magnetic sites and the oscillatory nature of the exchange interaction, the coupling between adjacent magnetic centers takes on a random sign and magnitude, leading to this disordered behavior. Accordingly, spin glass behavior emerges when the intercalation density differs from $x = 1/4$ or $x = 1/3$ in Fe_xNbS_2.[76–78] Furthermore, this spin glass order coexists with locally ordered AFM domains (Figure 9).[13] In an applied field, the glassy domains take on a net magnetization similar to a FM and are pinned by neighboring AFM domains, resulting in an exchange bias.[13] (We note that this picture neglects a possibly appreciable spin non-collinearity.)

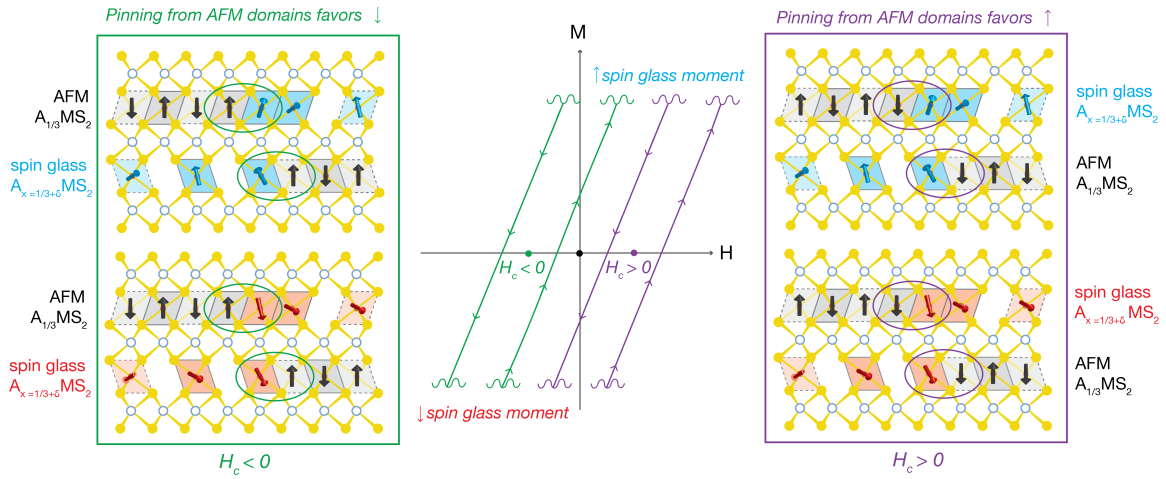

Figure 9: Schematic illustration of how disordered domains couple with ordered AFM domains in Fe_xNbS_2 with $x = 1/3+\delta$. Ordered AFM $\sqrt{3}\times\sqrt{3}$ superlattice domains are shown in black, while disordered domains exhibiting spin glass behavior are shown in red/blue. In an applied field, the glassy domains take on a net magnetization similar to a FM, as shown in the hysteresis curves. The pinning of the spin glass moments by the AFM domains results in an exchange bias field H_C, as illustrated in green and purple for $H_C < 0$ and $H_C > 0$, respectively, for relatively low-field measurements. Schematics reflect that the coupling between the spin glass and AFM domains is likely FM for both $\delta < 0$ and $\delta > 0$.[24]

Even in the absence of spin-glass order, Fe_xNbS_2 exhibits a complex magnetic phase space. The magnetic phase diagram of $Fe_{1/3}NbS_2$ contains four distinct phases as shown in Figure 10: an AFM phase (Phase I), an intermediate phase of unknown magnetic order (Phase II), a phase with a magnetization equal to half of the saturated moment (Phase III), and a paramagnetic phase (Phase IV).[79] The formation of the half saturation state, which corresponds to the metamagnetic transition at 17 T, results from the relatively large next-nearest neighbor coupling (i.e. in the adjacent plane) driving the formation of an up-up-up-down phase (shown in Figure 11), as predicted by density functional theory (DFT) calculations.[79] This appreciable next-nearest neighbor coupling further plays a role in the disputed ground state magnetic order of this material.

There are two proposed AFM orderings for the ground state in Fe_xNbS_2: the so-called stripe and zig-zag phases, each depicted in Figure 12. Separate neutron scattering studies provide conflicting evidence for a zig-zag and stripe ground state. However, these studies were performed on samples with slightly different intercalation densities of $x = 0.323$ and $x =$

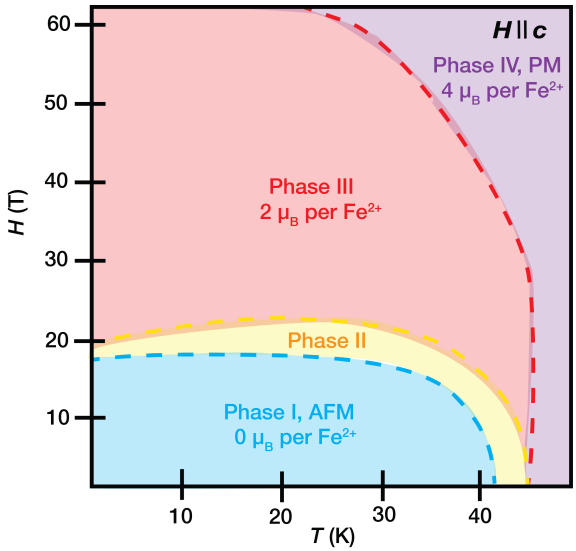

Figure 10: Phase diagram of $Fe_{1/3}NbS_2$ as revealed by torque magnetometry, heat capacity, and pulsed field magnetization measurements: an AFM phase (Phase I), an unknown intermediate phase (Phase II), an additional intermediate phase exhibiting a magnetic moment 1/2 times that of the saturated moment (Phase III), and a paramagnetic phase (Phase IV). The moments here are the overall moments arising from the (mis)oriented domains, while the Fe^{2+} centers retain individual moments of $4\mu_B/Fe^{2+}$ throughout.[79]

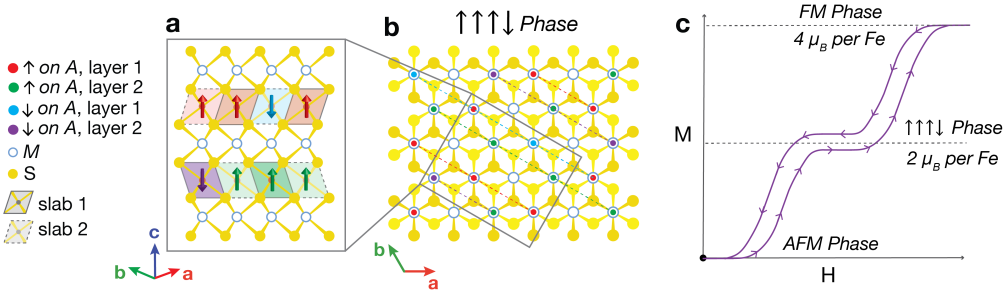

Figure 11: Side view (a) and top-down view (b) of the "up-up-up-down" magnetic order in $Fe_{1/3}NbS_2$, as suggested by computations to correspond to the metamagnetic transition leading to a characteristic plateau in the M vs. H curve (c) at a magnetization of 2 μ_B/Fe, half that expected of FM order. Hysteretic broadening is not expected for $x = 1/3$ and is shown for illustrative purposes.

0.297, respectively, suggesting that the magnetic order might be highly sensitive to the precise stoichiometry and perhaps even the sample uniformity.[2,80] More recent neutron diffraction studies instead indicate that under-intercalated samples ($x < 1/3$) display stripe order, and over-intercalated samples ($x > 1/3$) display zig-zag order.[81] Furthermore, DFT calculations conclude that the two phases are nearly degenerate, such that their relative stability depends on computational choices such as the Hubbard U-parameter.[82] Other computational work suggests that the stripe-phase is appreciably lower in energy and that the three-phase meta-magnetic structure is reproduced only for the stripe ground state, albeit using a relatively small parameterized model.[79] Accordingly, there is debate within the literature regarding the true nature of the ground state.

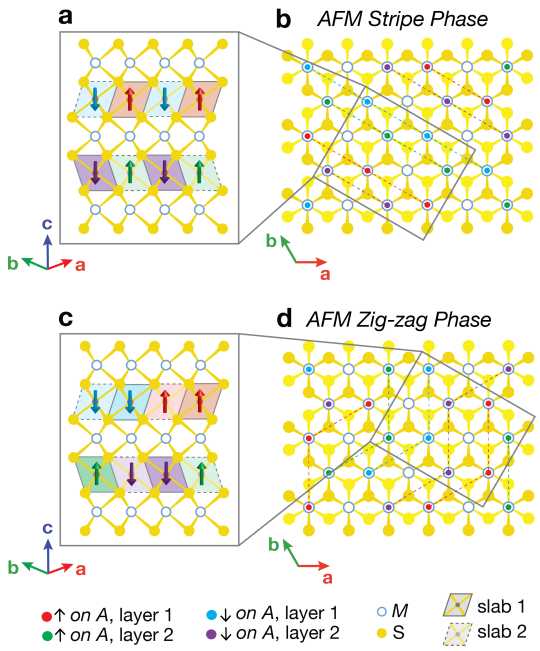

Figure 12: $Fe_{1/3}NbS_2$ exhibits two possible AFM ground states corresponding to different magnetic ordering on the $\sqrt{3} \times \sqrt{3}$ superlattice. Side view (a) and top-down view (b) of the stripe phase containing a collection of FM ordered stripe domains (illustrated with dotted lines) along $[1\bar{1}00]$. Side view (c) and top-down view (d) of the zig-zag phase containing ordered zig-zag regions (illustrated with dotted lines) with FM order along the axes perpendicular to a and b. (a, c) are side views of the region enclosed in the grey boxes in (b, d). The up-up-up-down phase in Figure 11 is identical to the stripe phase here, apart from an alternating spin order along the stripes which here contain exclusively down spins.

Regardless of whether the system adopts stripe or zig-zag domains, the magnetic ground

state of Fe_xNbS_2 exhibits three-fold rotational symmetry breaking, as is apparent in magnetic and transport measurements.[53] This is attributed to the formation of magnetic domains, which can be oriented along each of the three crystallographic directions. Each of these three symmetry-broken AFM states have different characteristic resistivity tensors[82] due to anisotropic scattering off the localized intercalant moments. Therefore, the observed low-current switching behavior may originate from current-driven interconversion between these three distinct AFM domains. This picture is supported by optical polarimetry measurements[16,53] and theoretical work showing that current pulses destabilize the AFM domains oriented parallel to the applied current.[82] Hence a complete understanding of the ground state magnetic order is essential to accurately model the resistive switching in this system; the magnitude of resistivity changes depends on the ground state and is expected to be larger for the stripe phase.[82] It has also been recently observed that applied spin currents have a non-local effect on Fe_xNbS_2, impacting the spin texture tens of microns away, much further than is achievable with typical magnon decay in metallic AFMs.[83] This non-local behavior was attributed to collective excitations of the system's complex spin textures (i.e. reorientation of and inter-conversion between stripe and zig-zag magnetic domains) driven by a large magnetoelastic coupling, which further highlights implications of the complex magnetic phase space of Fe_xNbS_2.

In addition to the ground state magnetic order, the degree of canting in Fe_xNbS_2 also merits further investigation. While Mössbauer spectroscopy has revealed Fe_xNbS_2 to be a primarily out-of-plane AFM,[23] the true magnetic order is likely more sophisticated. Some degree of canting may be present, as suggested by nuclear magnetic resonance and zero-field anisotropic magnetoresistance measurements,[24] as well as computational work[37] showing that collinear and non-collinear ordering are close in energy, due to competition between DM interactions and large MCAE. Furthermore, the mechanism driving the resistive switching depends on the degree of off-axis canting in these materials.[82] In the conventional spin–orbit torque mechanism, the exchange interaction between an applied spin current and the local

moments acts like an effective magnetic field.[84,85] This effective field imparts a torque on the magnetic moments, driving them to reorient. Thus, an appreciable in-plane component of the magnetic moments (i.e. spin canting) is required to facilitate strong coupling between the effective in-plane magnetic field and the magnetic order. However, this mechanism does not explain why remarkably low current densities are sufficient to mediate switching in $Fe_{1/3}NbS_2$. A different explanation for this phenomenon involves coupling mediated by intercalant disorder, namely via the formation of a spin glass.

While the resistive switching of Fe_xNbS_2 takes place even in the absence of the spin glass phase (i.e. above the spin glass freezing temperature and for $x = 1/3$), it does not exhibit the single pulse saturation and stability seen when the spin glass phase is present.[24] This suggests that spin glass order enables more efficient spin-polarized current rotation in Fe_xNbS_2. In the proposed mechanism, the collective motion of the spin glass imparts an additional spin torque on the Néel vector, effectively transferring angular momentum to the AFM domains.[16] It has further been noted that the sign of δ in $Fe_{1/3+\delta}NbS_2$ (i.e. if the sample has excess intercalants or vacancies) controls the direction of Néel vector rotation. This process is not completely understood and may relate to differences in the magnetic ordering as δ changes sign.[81]

In Fe_xNbS_2, the spin glass likely plays a crucial role in the material's resistive switching, serving as the first known direct application for a spin glass system. This compound further highlights that disorder, often seen as an undesirable source of dissipation or unpredictable behavior, can be leveraged to manipulate and foster technologically advantageous properties. However, much about this material remains unknown, including its debated ground state ordering, the nature of its metamagnetic plateau states, and the degree of off-axis canting. Additionally, while the low current switching behavior of Fe_xNbS_2 occurs at low temperatures, understanding its mechanism will help inform pursuits towards identifying other materials displaying switching behavior at higher temperatures. Investigating other systems for similar resistive switching may open doors to a room-temperature, low-current

AFM memory element with highly advantageous applications in energy-efficient electronics.

Chromium-Intercalated Niobium and Tantalum Sulfides

Studies of Cr_xNbS_2 and Cr_xTaS_2 materials have overwhelmingly focused on compounds with $x = 1/3$, which adopt a $\sqrt{3} \times \sqrt{3}$ superlattice and a noncentrosymmetric structure like other $T_{1/3}MS_2$ compounds described so far. Unlike their Fe-intercalated counterparts, the Cr analogues exhibit a magnetic easy plane in the ab plane (whereas the Fe-intercalated materials have an easy axis along c). The lack of inversion symmetry enables a DM interaction that competes with FM ordering and results in spin canting. As a result, both $Cr_{1/3}NbS_2$ and $Cr_{1/3}TaS_2$ exhibit chiral magnetic states that have made them fascinating platforms to study exotic spin textures. Specifically, at low fields, they have a chiral helimagnetic ground state composed of magnetic solitons. With larger applied fields, the distance between these solitons increases, illustrating the tunability of these chiral spin textures.

Comparing the properties of $Cr_{1/3}NbS_2$ and $Cr_{1/3}TaS_2$ reveals the effect of modifying the magnitude of the host lattice's SOC: going from NbS_2 to TaS_2 increases the relative strength of the DM interaction because the heavier metal imparts more SOC. As a result, the period of the chiral helimagnetic ground state, which is proportional to the ratio between the FM exchange interaction and the DM interaction,[86] decreases from $Cr_{1/3}NbS_2$ to $Cr_{1/3}TaS_2$.[18,19] As we shall discuss below, other magnetic properties, including T_C and critical field (above which the material enters a forced ferromagnetic state), are consistent with stronger magnetocrystalline anisotropy in $Cr_{1/3}TaS_2$.

Cr_xNbS_2

The first report of $Cr_{1/3}NbS_2$ was by Hulliger et al.,[1] revealing ferromagnetism with $T_C \sim 170$ K and an easy plane in the ab plane. Measurements showed μ_{eff} of 3.89 μ_B at saturation, consistent with $S = \frac{3}{2}$ from Cr^{3+}. The first reports of the possible helimagnetic ordering in

$Cr_{1/3}NbS_2$ at low temperatures were provided by Moriya et al.,[86] in which the magnetization data, as shown in Figure 13, was explained by DM interactions. The observed behavior was inconsistent with symmetric (Yoshimori-type) helimagnets, because of the metamagnetic behavior observed at the critical field.[40,87]

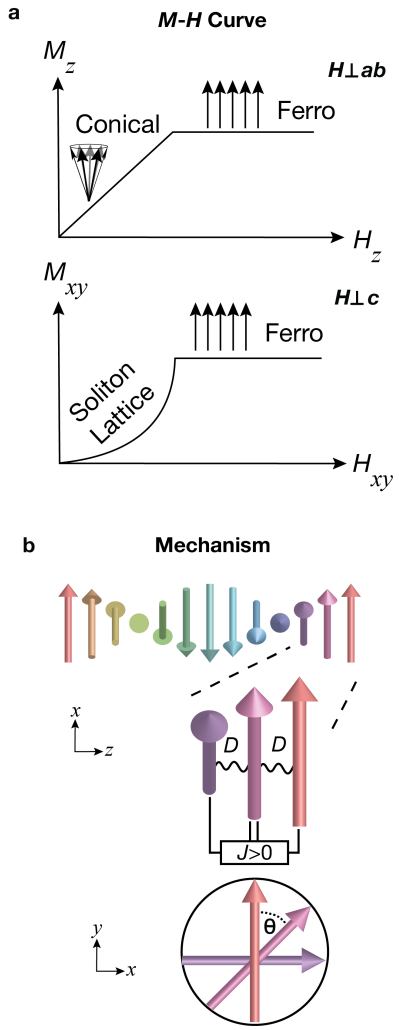

Figure 13: (a) Magnetization vs. magnetic field curves of a helimagnet with antisymmetric exchange when the field is applied perpendicular to the *ab*- and *c*-plane, respectively. (b) Schematic showing the interplay between ferromagnetic and DM interactions in a chiral helimagnet; these magnetic interactions lead to a characteristic angle between neighboring spins. Adapted from Togawa, Y.; Kousaka, Y.; Inoue, K.; Kishine, J. *J. Phys. Soc. Jpn.* **2016**, *85*, 112001.

The helimagnetic state of $Cr_{1/3}NbS_2$ was experimentally verified through small-angle neutron scattering measurements.[17] These neutron data showed a clear Bragg peak at Q

= 0.013 Å^{-1}, consistent with a helix of period ∼480 Å, as predicted previously.[17,86] Furthermore, these experiments found T_C to be closer to 127 K than ∼170 K, which had been suggested by earlier studies. Discrepancies in T_C were attributed to the large magnetization of $Cr_{1/3}NbS_2$ even at higher temperatures.[1,17] Togawa et al. confirmed the chiral helimagnetic phase with a period of 48 nm in $Cr_{1/3}NbS_2$, and also found using Lorentz TEM and small-angle electron diffraction that an applied magnetic field in the *ab* plane stabilizes an incommensurate chiral soliton lattice (CSL) that undergoes a continuous phase transition to a commensurate ferromagnetic state at higher magnetic fields.[18] This evolution from a chiral helimagnet (CHM) to CSL is evident in Lorentz TEM images (Figure 14c–g).

The interplay between different magnetic interactions in $Cr_{1/3}NbS_2$ produces a rich magnetic phase diagram,[88] (Figure 14) for $H \perp c$. Additional phases can be obtained with fields applied at different angles, such as a chiral conical phase and a tilted CSL.[89] These CHM and CSL phases are topologically protected because of the relativistic origin of the DM interaction that arises from noncentrosymmetry,[40] making them stable to defects such as those introduced by focused ion beams.[18] This robustness is promising for spintronics/microelectronics applications, in which the topological order might be used to store information and can be manipulated by initiating a phase transition (e.g. by changing temperature, magnetic field, strain,[90] or current flow[91]).

The topological order of $Cr_{1/3}NbS_2$ can be described by the 1D "winding number", w, as described by Equation 2.[92]

$$w = \frac{1}{2\pi}\int_{-\infty}^{\infty} dx \partial_x \phi \tag{2}$$

The winding number can be qualitatively understood by counting the complete "rotations" of the moments, i.e. the number of solitons along some chain, in this case the thickness of a $Cr_{1/3}NbS_2$ crystal; Figure 15 applies Equation 2 on an arbitrary lattice with a specific length to qualitatively show how the winding number can be obtained.

Charge and thermal transport measurements further elucidate the complex magnetic be-

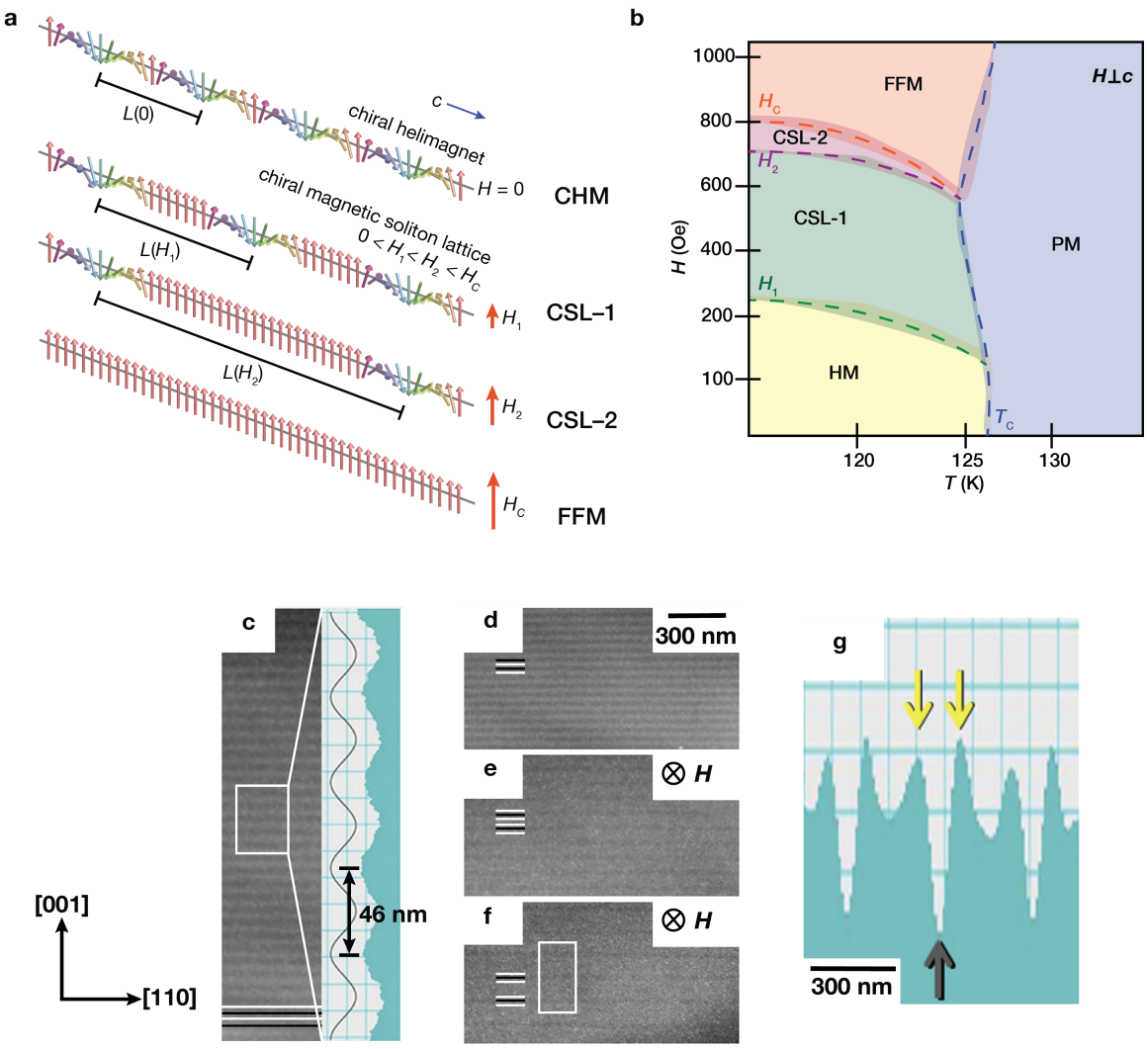

Figure 14: (a) Illustration of a right-handed chiral helimagnetic structure and its evolution towards a FFM. (b) Magnetic phase diagram of $Cr_{1/3}NbS_2$ with $H \perp c$. HM is helimagnetic ordering, CSL-1 is a soliton-dominated CSL, CSL-2 is a FM-dominated CSL, FFM is the forced ferromagnetic regime, and PM is the paramagnetic regime. Adapted from Han et al. *Phys. Rev. B* **2017**, *96*, 094439. (c) Underfocused Lorentz micrograph at 110 K showing CHM lines pattern, and a line profile of the contrast intensity in the white rectangle. The distance between black lines is the period of the solitons (approximately 46 nm). (d–f) Underfocused Lorentz micrographs of the same sample at 110 K in fields perpendicular to the c axis of 0, 0.208, and 0.224 T, respectively. (g) Line profile of the contrast intensity shown in the white rectangle in (f). The zero-field Lorentz TEM micrographs (c, d) show solitons that are closely spaced, while an applied magnetic field (e, f) effectively unwinds these solitons (increasing the distance between adjacent solitons), as shown by the period of the black lines. (c–g) Reprinted figures with permission from Togawa, Y.; Koyama, T.; Takayanagi, K.; Mori, S.; Kousaka, Y.; Akimitsu, J.; Nishihara, S.; Inoue, K.; Ovchinnikov, A. S.; Kishine, J. *Phys. Rev. Lett.* **2012**, *108*, 107202. Copyright 2012 by the American Physical Society.

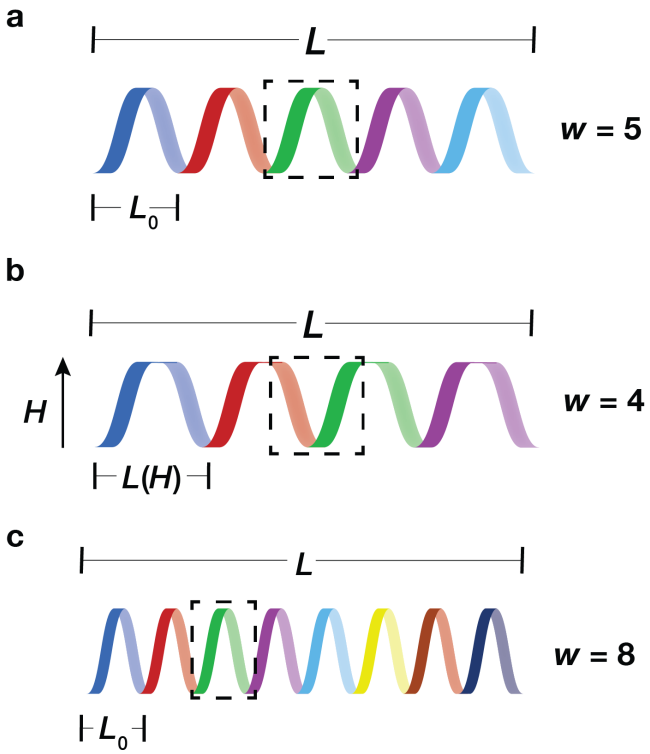

Figure 15: (a) Chiral helimagnet ground state for a particular lattice of a specific lattice size, which has a winding number of 5 in this case. (b) After a magnetic field is applied a chiral soliton lattice is formed with a reduced winding number due to the reduction of solitons. (c) A different material with stronger spin–orbit coupling, but same length as in (a), is able to host a higher winding number.

havior of $Cr_{1/3}NbS_2$ near T_C. Contrary to conventional metallic ferromagnets like Ni,[93–95] in which the resistivity uniformly decreases upon cooling, the resistivity in the *ab* plane exhibits an abrupt increase around T_C.[25] These results, along with other unusual MR behavior around T_C,[25,96–99] are indicative of complex transport properties of $Cr_{1/3}NbS_2$ which are not yet fully understood. Temperature-dependent variations in carrier concentrations and types from thermal transport and Hall measurements suggest the presence of multiple bands near the Fermi level, with relative contributions varying with temperature.[9,25]

Photoemission experiments confirmed the change in the electronic structure of $Cr_{1/3}NbS_2$ with magnetic ordering and indicate that $Cr_{1/3}NbS_2$ is a strongly correlated system in which the onset of ferromagnetism is closely tied to the electron itinerancy.[48,100] These data suggest that the rigid-band RKKY model does not accurately describe magnetic order in $Cr_{1/3}NbS_2$. Instead, the magnetism present in $Cr_{1/3}NbS_2$ appears to be closely intertwined with its electronic structure, implying that tuning its electronic structure may also lead to modulation of its magnetic properties.

Due to the presence of solitons, single crystals of $Cr_{1/3}NbS_2$ display discrete steps in magnetization with $H \perp c$.[101] These steps are not associated with the Barkhausen effect, which causes noise to occur in magnetization measurements due to the pinning and depinning of domains.[57] Instead, the discrete changes observed in $Cr_{1/3}NbS_2$ are attributed to the evolution of the CSL, i.e. field-induced changes in the winding number. Analogous features are also observed in transport measurements. Crystals of $Cr_{1/3}NbS_2$ with thicknesses greater than the length of the CHM, 48 nm, but thinner than the magnetic domain size, $\sim$1 μm, exhibit sharp drops in resistance with $H \perp c$.[102] The number of these steps is correlated with the total winding number of the $Cr_{1/3}NbS_2$ crystal, which corresponds to the thickness of the crystal divided by the length of the CHM, L_0. Hence, crystals thinner than L_0 with $w = 0$ did not display any sharp drops in resistance.

To date, the literature on stoichiometries of Cr_xNbS_2 with $x \neq 1/3$ is comparatively limited and also conflicting.[1,2,103–106] In these reports, disorder was found to suppress meta-

magnetic behavior, in addition to reducing the saturation moment, lowering T_C, and altering the oxidation states of intercalated Cr.[103–105] Moreover, for stoichiometries away from $Cr_{1/3}NbS_2$ earlier studies have reported both ferromagnetic and antiferromagnetic behavior.[1,2] The relative paucity and inconsistency of literature on these disordered structures encourages further studies into the impact of Cr stoichiometry on the magnetic properties of this family of materials, especially considering the precedent for disorder-controlled physics in Fe_xNbS_2.

Cr_xTaS_2

Like the Nb analogue, the most widely studied Cr_xTaS_2 material also has the formula $Cr_{1/3}TaS_2$, but its magnetic properties have not yet been studied in as much detail. Three recent studies show that the properties are qualitatively similar to $Cr_{1/3}NbS_2$, with analogous PM, CHM, CSL, and FFM states observed at different temperatures and applied magnetic fields. The shorter CHM period, higher T_C, and higher critical field of $Cr_{1/3}TaS_2$ compared to $Cr_{1/3}NbS_2$ appear to be consequences of larger SOC originating from the heavier host lattice. This strengthens the DM interaction, resulting in shorter solitons, and increases MCAE, resulting in larger T_C and critical field.

As first reported by Parkin and Friend, $Cr_{1/3}TaS_2$ exhibits magnetic ordering perpendicular to the c crystallographic axis like $Cr_{1/3}NbS_2$.[8,9] As with $Cr_{1/3}NbS_2$, the measured μ_{eff} value of 3.78 μ_B at saturation is consistent with the expected spin-only moment of Cr^{3+}. The presence of CHM and CSL phases was confirmed in recent studies from Obeysekera et al., Zhang et al., and Du et al., which also examined the evolution of the magnetic phase diagram.[19,26,107] Overall,Lorentz TEM and magnetotransport measurements reveal a qualitatively similar picture to $Cr_{1/3}NbS_2$: The CHM ground state is present below a certain transition temperature T_C at low fields. Upon applying higher $H \perp c$, a transition to a CSL state occurs, with the period of the CSL increasing with increasing H. Above the critical field, the material enters the FFM state.

Lorentz TEM studies have also revealed direct evidence of the chiral spin textures in $Cr_{1/3}TaS_2$.[19,107] Similar to $Cr_{1/3}NbS_2$, stripe patterns with alternating areas of light and dark contrast are present in images taken without an external magnetic field at 94 K or 22 K, respectively. Zhang et al. observed a period of 25 nm,[19] while Du et al. observed a shorter period of 15 nm.[107] This discrepancy may suggest differences in sample stoichiometry or homogeneity. Zhang et al. found that the period increased monotonically upon increasing H, with contrast vanishing above ∼12.7 kOe. This was attributed to evolution of a CSL state with increasing period and then a phase transition into the FFM state.

Magnetization measurements found $T_C \approx 140$ K at low fields, with a discontinuous peak moving to lower temperatures with higher $H \perp c$, disappearing completely above a critical field of ∼14 kOe.[19,26] Around the critical field, hysteresis on the order of 1 kOe was measured in the M vs. H curves of $Cr_{1/3}TaS_2$ at 2 K, compared to much smaller hysteresis (< 30 Oe) in $Cr_{1/3}NbS_2$.[25,86] Domed magnetoresistance was observed at low temperatures with small applied fields, consistent with alignment of solitons with the direction of H[26] Overall, the signatures of phase transitions from transport are consistent with those from magnetization measurements.

The magnetic phase diagrams of $Cr_{1/3}NbS_2$ and $Cr_{1/3}TaS_2$ appear qualitatively similar, with phase transitions occurring at higher fields in $Cr_{1/3}TaS_2$ (Figure 16).[19,88] Specifically, the values of $H \perp c$ required to transition between the CHM, CSL, and FFM phases are more than an order of magnitude greater in $Cr_{1/3}TaS_2$ than $Cr_{1/3}NbS_2$. In addition, T_C is more than 10 K higher in $Cr_{1/3}TaS_2$, consistent with stronger FM exchange compared with $Cr_{1/3}NbS_2$. These differences are all consistent with higher SOC from the host lattice increasing the strength of the DM interaction and MCAE.

Correlation between structural and magnetic domains in $Cr_{1/3}TaS_2$ have been investigated using dark-field TEM and magnetic force microscopy (MFM).[107] Left- and right-handed structural domains forming six-valent graphs were observed, similar to those found in $Fe_{1/3}TaS_2$.[10] MFM measurements revealed correspondence between structural and mag-

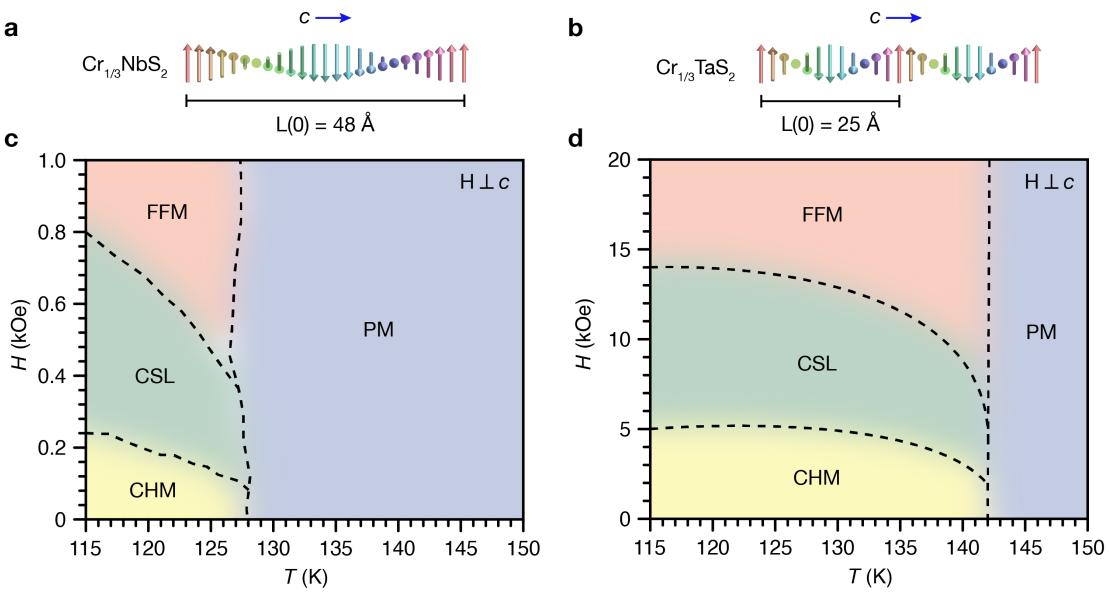

Figure 16: (a, b) Illustration of chiral helimagnetic states and their periods in $Cr_{1/3}NbS_2$ and $Cr_{1/3}TaS_2$, respectively. (c, d) Magnetic phase diagrams for $Cr_{1/3}NbS_2$ and $Cr_{1/3}TaS_2$, respectively, adapted from Han et al.[88] and Zhang et al.[19]

netic domains, with spiral spin textures undergoing a topological transition to concentric rings under applied fields. Such coupling between structural and magnetic chirality may enable tuning of magnetic textures in CHMs via manipulation of structural domains. Similar studies on $Cr_{1/3}NbS_2$ would be interesting to compare domain formation and investigate structural and magnetic coupling across these two materials.

Lastly, we note that the value of T_C for $Cr_{1/3}TaS_2$ varies across studies. Earlier studies reported $T_C \sim 110$ K, about 30 K lower than the results of Obeysekara et al. and Zhang et al.[8,9] Yamasaki et al. also reported $T_C \sim 110$ K from transport data for bulk crystals as well as a 65-nm thick exfoliated sample. On the other hand, magnetization measurements from Du et al. showed $T_C \sim 150$ K in bulk crystals.[107] The value of T_C may be sensitive to differences in stoichiometry or sample preparation conditions. A promising direction for future studies could be examining relationships between disorder, growth conditions, and magnetic transitions in more detail.

Outlook

Iron- and chromium-intercalated NbS_2 and TaS_2 compounds exhibit a variety of interesting magnetic behaviors depending on the identity of the intercalant and host lattice, as well as the precise intercalation stoichiometry. Studies to date have exploited a number of methods, including direct measurement of magnetic, electrical, and thermal properties; spectroscopic investigations of the electronic structure; imaging techniques, including TEM, Lorentz TEM, and MFM; and first-principles calculations to better understand these compounds.

Nevertheless, many promising avenues for further study remain. Below, we summarize some outstanding questions and directions of interest.

1. **Further investigation of exchange interactions.** Reports on some materials in this family, such as $Fe_{1/4}TaS_2$,[36] support RKKY as the predominant exchange mechanism mediating magnetic order. Other work on different materials, such as $Fe_{1/3}TaS_2$ and $Cr_{1/3}NbS_2$, have indicated more complex relationships between the electronic structure and magnetic properties.[25,48,60] It has been proposed that hybridization between the Fe intercalants and the TaS_2 host lattice is stronger for the $x = 1/3$ system than $x = 1/4$ because of higher intercalation density and inversion symmetry breaking in the $\sqrt{3} \times \sqrt{3}$ superlattice.[60] Still, a deeper understanding of the contribution of intercalant electronic states to the interplay between localized spins and itinerant bands could lead to avenues for fine-tuning magnetic properties in this class of materials.

2. **Precise determination of stoichiometry and superlattice structure.** Magnetic properties are often highly sensitive to the intercalation amount, as illustrated dramatically by small deviations from $x = 1/4$ in Fe_xTaS_2,[12] and $x = 1/3$ in Fe_xNbS_2.[13,24] However, not all studies have investigated precise compositions via elemental analysis techniques, such as energy-dispersive X-ray spectroscopy, electron energy loss spectroscopy, or inductively coupled plasma optical emission spectroscopy. In addition, the effects of non-stoichiometric host lattices (i.e. variation of the Nb or Ta and S stoi-

chiometries) remains to be systematically explored. Ideally, compositional data would be reported along with the magnetic properties, as well as the superlattice structure(s) observed. Since defective superlattices may not be apparent through diffraction techniques alone, correlation of electronic and magnetic properties with precise composition may improve reproducibility and uniformity, and lead to more comprehensive understanding of the impact of stoichiometry on magnetic properties.

3. **Controlling and imaging domain formation, and interplay between structural and magnetic domains.** The presence of microscopic domains with different compositions has been invoked to explain phenomena such as very large magnetoresistance in off-stoichiometric Fe_xTaS_2,[11] and exchange bias in $Fe_{1/3+\delta}NbS_2$.[13] While pronounced distinctions in the structural domain patterns of $Fe_{1/4}TaS_2$ and $Fe_{1/3}TaS_2$ have been observed,[10] direct imaging of the magnetic and structural domains in off-stoichiometric materials has not yet been reported. Furthermore, exploring the influence of composition and defects on domain wall density is also a worthy target of investigation. Recently, correlations between magnetic and structural domains in $Cr_{1/3}TaS_2$ were studied using a combination of MFM and dark-field TEM, suggesting that these techniques may be able to shed light on this interplay in related materials.

4. **Exploring a broader range of compositions.** Out of all of the T_xMS_2 materials discussed in this Perspective, detailed magnetic and transport properties have only been reported for a range of x in Fe_xTaS_2. Studies on Fe_xTaS_2 with $x \neq 1/4$ or $1/3$ and $Fe_{1/3 \pm \delta}NbS_2$ indicate that deviations from perfect superlattice stoichiometries can dramatically affect magnetic and transport properties due to the formation of disordered domains. Synthesizing and characterizing additional stoichiometries (including investigation of domain microstructure) could elucidate the origins of these phenomena. In addition, while chiral helimagnetism in the Cr-intercalated systems has been shown to be robust to scratch defects,[18] the effects of deviations in stoichiometry from $x = 1/3$

have not been explicitly explored. It would be worthwhile to investigate whether variation in values for T_C, H_C, and critical field across different reports could be traced back to slight differences in stoichiometry. Finally, related compounds with different intercalants and host lattices (including heavier chalcogens and alloyed intercalants) may reveal additional routes towards tuning magnetism.

5. **Reducing dimensionality.** Several studies have mechanically exfoliated $Fe_{1/4}TaS_2$, $Cr_{1/3}NbS_2$, and $Cr_{1/3}TaS_2$, obtaining flakes down to 40 or 50 nm in thickness that were used to fabricate devices for transport measurements.[11,102,108,109] Their properties were overall quite similar to the bulk analogues, but the magnetic behavior of thinner samples closer to the two-dimensional (2D) limit has not been reported until very recently.[110] Since magnetocrystalline anisotropy is necessary to stabilize magnetic order in 2D,[111] the TaS_2 materials may be especially appealing candidates due to larger SOC. The isolation of 2D analogues would also open up new opportunities for making heterostructures and more complex 2D devices, by taking full advantage of the degrees of freedom that are unique to atomically thin layers.

Acknowledgments

This material is based upon work supported by the Air Force Office of Scientific Research under AFOSR Award No. FA9550-20-1-0007. L.S.X. acknowledges support from the Arnold and Mabel Beckman Foundation and L'Oréal USA for postdoctoral fellowships. O.G. acknowledges support from a UCB Chancellor's Fellowship, NSF Graduate Research Fellowship grant DGE 1752814, and National GEM Consortium Fellowship. I.C. acknowledges support from a UCB Berkeley fellowship. D.K.B. acknowledges support from the W.M. Keck Foundation and the Gordon and Betty Moore Foundation EPiQS Initiative.

Competing Interests

The authors declare no competing interests.

References

(1) Hulliger, F.; Pobitschka, E. On the magnetic behavior of new $2H$-NbS_2-type derivatives. *J. Solid State Chem.* **1970**, *1*, 117–119.

(2) Van Laar, B.; Rietveld, H.; Ijdo, D. Magnetic and crystallographic structures of Me_xNbS_2 and Me_xTaS_2. *J. Solid State Chem.* **1971**, *3*, 154–160.

(3) Friend, R. H.; Beal, A. R.; Yoffe, A. D. Electrical and magnetic properties of some first row transition metal intercalates of niobium disulphide. *Philos. Mag.* **1977**, *35*, 1269–1287.

(4) Rao, G. V. S.; Shafer, M. W. In *Intercalated Layered Materials*; Lévy, F., Ed.; Springer Netherlands: Dordrecht, the Netherlands, 1979; pp 99–199.

(5) Wilson, J. A.; Yoffe, A. D. The transition metal dichalcogenides discussion and interpretation of the observed optical, electrical and structural properties. *Adv. Phys.* **1969**, *18*, 193–335.

(6) Di Salvo, F. J.; Hull Jr, G. W.; Schwartz, L. H.; Voorhoeve, J. M.; Waszczak, J. V. Metal intercalation compounds of TaS_2: Preparation and properties. *J. Chem. Phys.* **1973**, *59*, 1922–1929.

(7) Marseglia, E. A. Transition Metal Dichalcogenides and Their Intercalates. *Int. Rev. Phys. Chem.* **1983**, *3*, 177–216.

(8) Parkin, S. S.; Friend, R. H. 3d transition-metal intercalates of the niobium and tantalum dichalcogenides II. Transport properties. *Philos. Mag. B* **1980**, *41*, 95–112.

(9) Parkin, S. S.; Friend, R. H. 3d transition-metal intercalates of the niobium and tantalum dichalcogenides I. Magnetic properties. *Philos. Mag. B* **1980**, *41*, 65–93.

(10) Horibe, Y.; Yang, J.; Cho, Y. H.; Luo, X.; Kim, S. B.; Oh, Y. S.; Huang, F. T.; Asada, T.; Tanimura, M.; Jeong, D.; Cheong, S. W. Color theorems, chiral domain topology, and magnetic properties of Fe_xTaS_2. *J. Am. Chem. Soc.* **2014**, *136*, 8368–8373.

(11) Hardy, W. J.; Chen, C. W.; Marcinkova, A.; Ji, H.; Sinova, J.; Natelson, D.; Morosan, E. Very large magnetoresistance in $Fe_{0.28}TaS_2$ single crystals. *Phys. Rev. B* **2015**, *91*, 054426.

(12) Chen, C. W.; Chikara, S.; Zapf, V. S.; Morosan, E. Correlations of crystallographic defects and anisotropy with magnetotransport properties in Fe_xTaS_2 single crystals ($0.23 \leq x \leq 0.35$). *Phys. Rev. B* **2016**, *94*, 054406.

(13) Maniv, E.; Murphy, R. A.; Haley, S. C.; Doyle, S.; John, C.; Maniv, A.; Ramakrishna, S. K.; Tang, Y.-L.; Ercius, P.; Ramesh, R.; Reyes, A. P.; Long, J. R.; Analytis, J. G. Exchange bias due to coupling between coexisting antiferromagnetic and spin-glass orders. *Nat. Phys.* **2021**, *17*, 525–530.

(14) Morosan, E.; Zandbergen, H. W.; Li, L.; Lee, M.; Checkelsky, J. G.; Heinrich, M.; Siegrist, T.; Ong, N. P.; Cava, R. J. Sharp switching of the magnetization in $Fe_{1/4}TaS_2$. *Phys. Rev. B* **2007**, *75*, 104401.

(15) Checkelsky, J. G.; Lee, M.; Morosan, E.; Cava, R. J.; Ong, N. P. Anomalous Hall effect and magnetoresistance in the layered ferromagnet $Fe_{1/4}TaS_2$: The inelastic regime. *Phys. Rev. B* **2008**, *77*, 014433.

(16) Nair, N. L.; Maniv, E.; John, C.; Doyle, S.; Orenstein, J.; Analytis, J. G. Electrical switching in a magnetically intercalated transition metal dichalcogenide. *Nat. Mater.* **2020**, *19*, 153–157.

(17) Miyadai, T.; Kikuchi, K.; Kondo, H.; Sakka, S.; Arai, M.; Ishikawa, Y. Magnetic Properties of $Cr_{1/3}NbS_2$. *J. Phys. Soc. Jpn.* **1983**, *52*, 1394–1401.

(18) Togawa, Y.; Koyama, T.; Takayanagi, K.; Mori, S.; Kousaka, Y.; Akimitsu, J.; Nishihara, S.; Inoue, K.; Ovchinnikov, A. S.; Kishine, J. Chiral magnetic soliton lattice on a chiral helimagnet. *Phys. Rev. Lett.* **2012**, *108*, 107202.

(19) Zhang, C. et al. Chiral Helimagnetism and One-Dimensional Magnetic Solitons in a Cr-Intercalated Transition Metal Dichalcogenide. *Adv. Mater.* **2021**, *33*, 2101131.

(20) Eibschütz, M.; Mahajan, S.; DiSalvo, F. J.; Hull, G. W.; Waszczak, J. V. Ferromagnetism in metallic intercalated compounds Fe_xTaS_2 ($0.20 \leq x \leq 0.34$). *J. Appl. Phys.* **1981**, *52*, 2098–2100.

(21) Narita, H.; Ikuta, H.; Hinode, H.; Uchida, T.; Ohtani, T.; Wakihara, M. Preparation and Physical Properties of Fe_xTaS_2 ($0.15 \leq x \leq 0.50$) Compounds. *J. Solid State Chem.* **1994**, *108*, 148–151.

(22) Mangelsen, S.; Hansen, J.; Adler, P.; Schnelle, W.; Bensch, W.; Mankovsky, S.; Polesya, S.; Ebert, H. Large Anomalous Hall Effect and Slow Relaxation of the Magnetization in $Fe_{1/3}TaS_2$. *J. Phys. Chem. C* **2020**, *124*, 24984–24994.

(23) Gorochov, O.; Blanc-soreau, A. L.; Rouxel, J.; Imbert, P.; Jehanno, G. Transport properties, magnetic susceptibility and Mössbauer spectroscopy of $Fe_{0.25}NbS_2$ and $Fe_{0.33}NbS_2$. *Philos. Mag. B* **1981**, *43*, 621–634.

(24) Maniv, E.; Nair, N. L.; Haley, S. C.; Doyle, S.; John, C.; Cabrini, S.; Maniv, A.; Ramakrishna, S. K.; Tang, Y.-L.; Ercius, P.; Ramash, R.; Tserkovnyak, Y.; Reyes, A. P.; Analytis, J. G. Antiferromagnetic switching driven by the collective dynamics of a coexisting spin glass. *Sci. Adv.* **2021**, *7*, eabd8452.

(25) Ghimire, N. J.; McGuire, M. A.; Parker, D. S.; Sipos, B.; Tang, S.; Yan, J.-Q.; Sales, B. C.; Mandrus, D. Magnetic phase transition in single crystals of the chiral helimagnet $Cr_{1/3}NbS_2$. *Phys. Rev. B* **2013**, *87*, 104403.

(26) Obeysekera, D.; Gamage, K.; Gao, Y.; Cheong, S.; Yang, J. The Magneto-Transport Properties of $Cr_{1/3}TaS_2$ with Chiral Magnetic Solitons . *Adv. Electron. Mater.* **2021**, *7*, 2100424.

(27) Trichet, L.; Cousseau, J.; Rouxel, J. Les systemes Fe-ZrS_2 et Co-ZrS_2. Structure M_xZrS_2. *C. R. Seances Acad. Sci., Ser. C* **1972**, *274*, 394–397.

(28) Liu, X.-C.; Zhao, S.; Sun, X.; Deng, L.; Zou, X.; Hu, Y.; Wang, Y.-X.; Chu, C.-W.; Li, J.; Wu, J.; Ke, F.-S.; Ajayan, P. M. Spontaneous Self-Intercalation of Copper Atoms into Transition Metal Dichalcogenides. *Science Advances 6*, eaay4092.

(29) Meerschaut, A.; Deudon, C. Crystal Structure Studies of the $3R$-$Nb_{1.09}S_2$ and the $2H$-$NbSe_2$ Compounds: Correlation between Nonstoichiometry and Stacking Type (= Polytypism). *Materials Research Bulletin* **2001**, *36*, 1721–1727.

(30) Gotoh, Y.; Akimoto, J.; Oosawa, Y. Crystal Structure of $3R$-$Ta_{1.08}S_2$. *Journal of Alloys and Compounds* **1998**, *270*, 115–118.

(31) Bark, H.; Choi, Y.; Jung, J.; Kim, J. H.; Kwon, H.; Lee, J.; Lee, Z.; Cho, J. H.; Lee, C. Large-area niobium disulfide thin films as transparent electrodes for devices based on two-dimensional materials. *Nanoscale* **2018**, *10*, 1056–1062.

(32) Rumble, J. R., Ed. *CRC Handbook of Chemistry and Physics*, 102nd ed.; CRC Press: Boca Raton, 2019; Chapter 12.

(33) Chhowalla, M.; Shin, H. S.; Eda, G.; Li, L.-J.; Loh, K. P.; Zhang, H. The chemistry of two-dimensional layered transition metal dichalcogenide nanosheets. *Nat. Chem.* **2013**, *5*, 263–275.

(34) Bell, M. G.; Liang, W. Y. Electron energy loss studies in solids; The transition metal dichalcogenides. *Adv. Phys.* **1976**, *25*, 53–86.

(35) Clark, W. B. Structural and photoemission studies of some transition metal intercalates of NbS_2. *J. Phys. C Solid State Phys.* **1976**, *9*, L693–L696.

(36) Ko, K. T.; Kim, K.; Kim, S. B.; Kim, H. D.; Kim, J. Y.; Min, B. I.; Park, J. H.; Chang, F. H.; Lin, H. J.; Tanaka, A.; Cheong, S. W. RKKY frromagnetism with Ising-like spin states in intercalated $Fe_{1/4}TaS_2$. *Phys. Rev. Lett.* **2011**, *107*, 247201.

(37) Mankovsky, S.; Polesya, S.; Ebert, H.; Bensch, W. Electronic and magnetic properties of $2H$-NbS_2 intercalated by $3d$ transition metals. *Phys. Rev. B* **2016**, *94*, 184430.

(38) Du Trémolet de Lacheisserie, E.; Gignoux, D.; Schlenker, M. *Magnetism*; Kluwer Academic Publishers: Norwell, 2002; pp 311–320.

(39) Kittel, C. *Introduction to Solid State Physics*, 8th ed.; John Wiley & Sons: New York, NY, 2005; Chapter 12, pp 323–360.

(40) Togawa, Y.; Kousaka, Y.; Inoue, K.; Kishine, J.-i. Symmetry, Structure, and Dynamics of Monoaxial Chiral Magnets. *J. Phys. Soc. Jpn.* **2016**, *85*, 112001.

(41) Jiang, X.; Liu, Q.; Xing, J.; Liu, N.; Guo, Y.; Liu, Z.; Zhao, J. Recent progress on 2D magnets: Fundamental mechanism, structural design and modification. *Appl. Phys. Rev.* **2021**, *8*, 031305.

(42) Ashcroft, N. W.; Mermin, N. D. *Solid State Physics*; Holt, Rinehart and Winston: New York, NY, 1976.

(43) Cox, P. A. *The Electronic Structure and Chemistry of Solids*; Oxford University Press: Oxford, U.K., 1987.

(44) Orchard, A. F. *Magnetochemistry*; Oxford University Press: Oxford, U.K., 2003.

(45) Ruderman, M. A.; Kittel, C. Indirect Exchange Coupling of Nuclear Magnetic Moments by Conduction Electrons. *Phys. Rev.* **1954**, *96*, 99–102.

(46) Kasuya, T. A theory of metallic ferro-and antiferromagnetism on Zener's model. *Prog. Theor. Phys.* **1956**, *16*, 45–57.

(47) Yosida, K. Magnetic properties of Cu–Mn alloys. *Phys. Rev.* **1957**, *106*, 893.

(48) Sirica, N.; Vilmercati, P.; Bondino, F.; Pis, I.; Nappini, S.; Mo, S. K.; Fedorov, A. V.; Das, P. K.; Vobornik, I.; Fujii, J.; Li, L.; Sapkota, D.; Parker, D. S.; Mandrus, D. G.; Mannella, N. The nature of ferromagnetism in the chiral helimagnet $Cr_{1/3}NbS_2$. *Commun. Phys.* **2020**, *3*, 65.

(49) Dzyaloshinsky, I. A thermodynamic theory of "weak" ferromagnetism of antiferromagnetics. *J. Phys. Chem. Solids* **1958**, *4*, 241–255.

(50) Moriya, T. Anisotropic Superexchange Interaction and Weak Ferromagnetism. *Phys. Rev.* **1960**, *120*, 91–98.

(51) Izyumov, Y. A. Modulated, or long-periodic, magnetic structures of crystals. *Sov. Phys. Usp.* **1984**, *24*, 845–867.

(52) Jena, J.; Göbel, B.; Kumar, V.; Mertig, I.; Felser, C.; Parkin, S. Evolution and competition between chiral spin textures in nanostripes with D_{2d} symmetry. *Sci. Adv.* **2020**, *6*, eabc0723.

(53) Little, A.; Lee, C.; John, C.; Doyle, S.; Maniv, E.; Nair, N. L.; Chen, W.; Rees, D.; Venderbos, J. W.; Fernandes, R. M.; Analytis, J. G.; Orenstein, J. Three-state nematicity in the triangular lattice antiferromagnet $Fe_{1/3}NbS_2$. *Nat. Mater.* **2020**, *19*, 1062–1067.

(54) Choe, J.; Lee, K.; Huang, C.-L.; Trivedi, N.; Morosan, E. Magnetotransport in Fe-intercalated TS_2: Comparison between Ti and Ta. *Phys. Rev. B* **2019**, *99*, 064420.

(55) Zhang, C.; Yuan, Y.; Wang, M.; Li, P.; Zhang, J.; Wen, Y.; Zhou, S.; Zhang, X.-X. Critical behavior of intercalated quasi-van der Waals ferromagnet $Fe_{0.26}TaS_2$. *Phys. Rev. Mater.* **2019**, *3*, 114403.

(56) Specht, F. Indirect Exchange Interaction in the Rare-Earth Metals. *Phys. Rev.* **1967**, *162*, 389–398.

(57) Spaldin, N. A. *Magnetic Materials: Fundamentals and Applications*, 2nd ed.; Cambridge University Press, pp 65–95.

(58) Dijkstra, J.; Zijlema, P. J.; Haas, C.; Groot, D. Band-structure calculations of $Fe_{1/3}TaS_2$ and $Mn_{1/3}TaS_2$, and transport and magnetic properties of $Fe_{0.28}TaS_2$. *J. Phys.: Condens. Matter* **1989**, *1*, 6363–6379.

(59) Vannette, M. D.; Yeninas, S.; Morosan, E.; Cava, R. J.; Prozorov, R. Local-moment ferromagnetism and unusual magnetic domains in $Fe_{1/4}TaS_2$ crystals. *Phys. Rev. B* **2009**, *80*, 024421.

(60) Fan, S.; Manuel, I.; al Wahish, A.; O'Neal, K. R.; Smith, K. A.; Won, C. J.; Kim, J. W.; Cheong, S.-W.; Haraldsen, J. T.; Musfeldt, J. L. Electronic chirality in the metallic ferromagnet $Fe_{1/3}TaS_2$. *Phys. Rev. B* **2017**, *96*, 205119.

(61) Zheng, G.; Wang, M.; Zhu, X.; Tan, C.; Wang, J.; Albarakati, S.; Aloufi, N.; Algarni, M.; Farrar, L.; Wu, M.; Yao, Y.; Tian, M.; Zhou, J.; Wang, L. Tailoring Dzyaloshinskii–Moriya interaction in a transition metal dichalcogenide by dual-intercalation. *Nat. Commun.* **2021**, *12*, 3639.

(62) You, C.-Y. Curie temperature of ultrathin ferromagnetic layer with Dzyaloshinskii–Moriya interaction. *J. Appl. Phys.* **2014**, *116*, 053902.

(63) Baibich, M. N.; Broto, J. M.; Fert, A.; Van Dau, F. N.; Petroff, F.; Etienne, P.;

Creuzet, G.; Friederich, A.; Chazelas, J. Giant Magnetoresistance of (001)Fe/(001)Cr Magnetic Superlattices. *Physical Review Letters* **1988**, *61*, 2472–2475.

(64) Binasch, G.; Grünberg, P.; Saurenbach, F.; Zinn, W. Enhanced Magnetoresistance in Layered Magnetic Structures with Antiferromagnetic Interlayer Exchange. *Physical Review B* **1989**, *39*, 4828–4830.

(65) Parkin, S. S. P. Giant Magnetoresistance in Magnetic Nanostructures. *Annual Review of Materials Science* **1995**, *25*, 357–388.

(66) Gil, W.; Görlitz, D.; Horisberger, M.; Kötzler, J. Magnetoresistance anisotropy of polycrystalline cobalt films: Geometrical-size and domain effects. *Phys. Rev. B* **2005**, *72*, 134401.

(67) Raquet, B.; Viret, M.; Broto, J. M.; Sondergard, E.; Cespedes, O.; Mamy, R. Magnetic resistivity and electron–magnon scattering in 3d ferromagnets. *J. Appl. Phys.* **2002**, *91*, 8129–8131.

(68) Choi, Y. J.; Kim, S. B.; Asada, T.; Park, S.; Wu, W.; Horibe, Y.; Cheong, S.-W. Giant magnetic coercivity and ionic superlattice nano-domains in $Fe_{0.25}TaS_2$. *Europhys. Lett.* **2009**, *86*, 37012.

(69) Yamamura, Y.; Moriyama, S.; Tsuji, T.; Iwasa, Y.; Koyano, M.; Katayama, S.; Ito, M. Heat capacity and phase transition of Fe_xNbS_2 at low temperature. *J. Alloys Compd.* **2004**, *383*, 338–341.

(70) Wannier, G. H. Antiferromagnetism. the triangular ising net. *Physical Review* **1950**, *79*, 357.

(71) Wannier, G. H. Antiferromagnetism. the triangular ising net. *Phys. Rev. B* **1973**, *7*, 5017.

(72) Binder, K.; Young, A. P. Spin glasses: Experimental facts, theoretical concepts, and open questions. *Rev. Mod. Phys.* **1986**, *58*, 801.

(73) Cannella, V.; Mydosh, J. A. Magnetic ordering in gold-iron alloys. *Phys. Rev. B* **1972**, *6*, 4220.

(74) Bouchiat, H.; Monod, P. Remanent magnetisation properties of the spin glass phase. *J. Magn. Magn. Mater.* **1982**, *30*, 175–191.

(75) Tholence, J.; Tournier, R. Susceptibility and remanent magnetization of a spin glass. *J. Phys. Colloq.* **1974**, *35*, C4–229.

(76) Tsuji, T.; Yamamura, Y.; Koyano, M.; Katayama, S.; Ito, M. Thermodynamic and magnetic properties of intercalated layered compounds Fe_xNbS_2. *J. Alloys Compd.* **2001**, *317*, 213–216.

(77) Koyano, M.; Watanabe, H.; Yamamura, Y.; Tsuji, T.; Katayama, S. Magnetic and Raman scattering studies on intercalation compounds Fe_xNbS_2. *Mol. Cryst. Liq. Cryst.* **2000**, *341*, 33–38.

(78) Doi, N.; Tazuke, Y. Spin glass phases in $2H$-Fe_xNbS_2. *J. Phys. Soc. Jpn.* **1991**, *60*, 3980–3981.

(79) Haley, S. C.; Weber, S. F.; Cookmeyer, T.; Parker, D. E.; Maniv, E.; Maksimovic, N.; John, C.; Doyle, S.; Maniv, A.; Ramakrishna, S. K., et al. Half-magnetization plateau and the origin of threefold symmetry breaking in an electrically switchable triangular antiferromagnet. *Phys. Rev. Res.* **2020**, *2*, 043020.

(80) Suzuki, T.; Ikeda, S.; Richardson, J.; Yamaguchi, Y. Magnetic structure of $Fe_{1/3}NbS_2$. Proc. 5th International Symposium on Advanced Nuclear Energy Research. 1993; pp 343–346, JAERI-M–93-228.

(81) Wu, S.; Xu, Z.; Haley, S. C.; Weber, S. F.; Acharya, A.; Maniv, E.; Qiu, Y.; Aczel, A.; Neaton, J. B.; Analytis, J. G.; Birgeneau, R. J. Highly tunable magnetic phases in transition metal dichalcogenide $Fe_{1/3+\delta}NbS_2$. *arXiv preprint* **2021**, *arXiv:2106.01341*.

(82) Weber, S. F.; Neaton, J. B. Origins of anisotropic transport in the electrically switchable antiferromagnet $Fe_{1/3}NbS_2$. *Phys. Rev. B* **2021**, *103*, 214439.

(83) Haley, S. C.; Maniv, E.; Cookmeyer, T.; Torres-Londono, S.; Aravinth, M.; Moore, J.; Analytis, J. G. Long-range, Non-local Switching of Spin Textures in a Frustrated Antiferromagnet. *arXiv preprint* **2021**, arXiv:2111.09882.

(84) Gomonay, H. V.; Loktev, V. M. Spin transfer and current-induced switching in antiferromagnets. *Phys. Rev. B* **2010**, *81*, 144427.

(85) Gomonay, O.; Jungwirth, T.; Sinova, J. Concepts of antiferromagnetic spintronics. *Phys. Status Solidi Rapid Res. Lett.* **2017**, *11*, 1700022.

(86) Moriya, T.; Miyadai, T. Evidence for the helical spin structure due to antisymmetric exchange interaction in $Cr_{1/3}NbS_2$. *Solid State Commun.* **1982**, *42*, 209–212.

(87) Nagamiya, T. Helical Spin Ordering—1 Theory of Helical Spin Configurations. *Solid State Phys.* **1968**, *20*, 305–411.

(88) Han, H.; Zhang, L.; Sapkota, D.; Hao, N.; Ling, L.; Du, H.; Pi, L.; Zhang, C.; Mandrus, D. G.; Zhang, Y. Tricritical point and phase diagram based on critical scaling in the monoaxial chiral helimagnet $Cr_{1/3}NbS_2$. *Phys. Rev. B* **2017**, *96*, 094439.

(89) Yonemura, J.-i.; Shimamoto, Y.; Kida, T.; Yoshizawa, D.; Kousaka, Y.; Nishihara, S.; Goncalves, F. J. T.; Akimitsu, J.; Inoue, K.; Hagiwara, M.; Togawa, Y. Magnetic solitons and magnetic phase diagram of the hexagonal chiral crystal $CrNb_3S_6$ in oblique magnetic fields. *Phys. Rev. B* **2017**, *96*, 184423.

(90) Paterson, G. W.; Tereshchenko, A. A.; Nakayama, S.; Kousaka, Y.; Kishine, J.; McVitie, S.; Ovchinnikov, A. S.; Proskurin, I.; Togawa, Y. Tensile deformations of the magnetic chiral soliton lattice probed by Lorentz transmission electron microscopy. *Phys. Rev. B* **2020**, *101*, 184424.

(91) Inui, A.; Aoki, R.; Nishiue, Y.; Shiota, K.; Kousaka, Y.; Shishido, H.; Hirobe, D.; Suda, M.; Ohe, J.-i.; Kishine, J.-i.; Yamamoto, H. M.; Togawa, Y. Chirality-Induced Spin-Polarized State of a Chiral Crystal $CrNb_3S_6$. *Phys. Rev. Lett.* **2020**, *124*, 166602.

(92) Braun, H.-B. Topological effects in nanomagnetism: from superparamagnetism to chiral quantum solitons. *Adv. Phys.* **2012**, *61*, 1–116.

(93) Goodings, D. A. Electrical Resistivity of Ferromagnetic Metals at Low Temperatures. *Phys. Rev.* **1963**, *132*, 542–558.

(94) Kasuya, T. Electrical Resistance of Ferromagnetic Metals. *Prog. Theor. Phys.* **1956**, *16*, 58–63.

(95) R., B. R.; K., D. S. The temperature dependence of the resistivity of ferromagnetic metals. *Proc. R. Soc. Lond. A* **1961**, *263*, 473–482.

(96) Togawa, Y.; Kousaka, Y.; Nishihara, S.; Inoue, K.; Akimitsu, J.; Ovchinnikov, A. S.; Kishine, J. Interlayer Magnetoresistance due to Chiral Soliton Lattice Formation in Hexagonal Chiral Magnet $CrNb_3S_6$. *Phys. Rev. Lett.* **2013**, *111*, 197204.

(97) Hicken, T. J.; Hawkhead, Z.; Wilson, M. N.; Huddart, B. M.; Hall, A. E.; Balakrishnan, G.; Wang, C.; Pratt, F. L.; Clark, S. J.; Lancaster, T. Energy-gap driven low-temperature magnetic and transport properties in $Cr_{1/3}MS_2$ (M = Nb, Ta). *Phys. Rev. B* **2022**, *105*, L060407.

(98) Sirica, N.; Hedayat, H.; Bugini, D.; Koehler, M. R.; Li, L.; Parker, D. S.; Mandrus, D. G.; Dallera, C.; Carpene, E.; Mannella, N. Disentangling electronic, lat-

tice, and spin dynamics in the chiral helimagnet $Cr_{1/3}NbS_2$. *Phys. Rev. B* **2021**, *104*, 174426.

(99) Mayoh, D. A.; Bouaziz, J.; Hall, A. E.; Staunton, J. B.; Lees, M. R.; Balakrishnan, G. Giant topological and planar Hall effect in $Cr_{1/3}NbS_2$. *Phys. Rev. Res.* **2022**, *4*, 013134.

(100) Sirica, N. et al. Electronic structure of the chiral helimagnet and 3 d -intercalated transition metal dichalcogenide $Cr_{1/3}NbS_2$. *Phys. Rev. B* **2016**, *94*, 075141.

(101) Tsuruta, K.; Mito, M.; Kousaka, Y.; Akimitsu, J.; Kishine, J.-i.; Togawa, Y.; Ohsumi, H.; Inoue, K. Discrete Change in Magnetization by Chiral Soliton Lattice Formation in the Chiral Magnet $Cr_{1/3}NbS_2$. *J. Phys. Soc. Jpn.* **2016**, *85*, 013707.

(102) Wang, L.; Chepiga, N.; Ki, D.-K.; Li, L.; Li, F.; Zhu, W.; Kato, Y.; Ovchinnikova, O. S.; Mila, F.; Martin, I.; Mandrus, D.; Morpurgo, A. F. Controlling the Topological Sector of Magnetic Solitons in Exfoliated $Cr_{1/3}NbS_2$ Crystals. *Phys. Rev. Lett.* **2017**, *118*, 257203.

(103) Dyadkin, V.; Mushenok, F.; Bosak, A.; Menzel, D.; Grigoriev, S.; Pattison, P.; Chernyshov, D. Structural disorder versus chiral magnetism in $Cr_{1/3}NbS_2$. *Phys. Rev. B* **2015**, *91*, 184205.

(104) Ogloblichev, V. V.; Piskunov, Y. V.; Mushenok, F. B. Magnetic order in the structurally disordered helicoidal magnet $Cr_{1/3}NbS_2$: NMR at ^{53}Cr nuclei. *J. Exp. Theor. Phys.* **2017**, *125*, 317–322.

(105) Sidorov, V. A.; Petrova, A. E.; Pinyagin, A. N.; Kolesnikov, N. N.; Khasanov, S. S.; Stishov, S. M. Physical properties and phase diagram of the magnetic compound $Cr_{0.26}NbS_{1.74}$ at high pressures. *J. Exp. Theor. Phys.* **2016**, *122*, 1047–1051.

(106) Mao, Q.; Wang, Y.; Li, R.; Qian, J.; Wang, H.; Chen, B.; Ding, J.; Khan, R.; Hao, H.;

Yang, J. Magnetic and Critical Properties of $Cr_{1/3}NbS_{1.86}$ with T_C = 56 K. *Phys. Status Solidi RRL* **2022**, *16*, 2100410.

(107) Du, K.; Huang, F.-t.; Kim, J.; Lim, S. J.; Gamage, K.; Yang, J.; Mostovoy, M.; Garlow, J.; Han, M.-G.; Zhu, Y.; Cheong, S.-W. Topological spin/structure copulings in layered chiral magnet $Cr_{1/3}TaS_2$: The discovery of spiral magnetic superstructure. *Proc. Natl. Acad. Sci.* **2021**, *118*, e2023337118.

(108) Yamasaki, Y.; Moriya, R.; Arai, M.; Masubuchi, S.; Pyon, S.; Tamegai, T.; Ueno, K.; Machida, T. Exfoliation and van der Waals heterostructure assembly of intercalated ferromagnet $Cr_{1/3}TaS_2$. *2D Mater.* **2017**, *4*, 041007.

(109) Cai, R.; Xing, W.; Zhou, H.; Li, B.; Chen, Y.; Yao, Y.; Ma, Y.; Xie, X. C.; Jia, S.; Han, W. Anomalous Hall Effect Mechanisms in the Quasi-Two-Dimensional van Der Waals Ferromagnet $Fe_{0.29}TaS_2$. *Phys. Rev. B* **2019**, *100*, 054430.

(110) Husremović, S.; Inzani, K.; Groschner, C. K.; Craig, I. M.; Bustillo, K. C.; Kazmierczak, N. P.; Syndikus, J.; Van Winkle, M.; Aloni, S.; Taniguchi, T.; Watanabe, K.; Griffin, S. M.; Bediako, D. K. Hard ferromagnetism down to the thinnest limit of iron-intercalated tantalum disulfide. 2022; `https://arxiv.org/abs/2203.05747`.

(111) Gibertini, M.; Koperski, M.; Morpurgo, A. F.; Novoselov, K. S. Magnetic 2D materials and heterostructures. *Nat. Nanotechnol.* **2019**, *14*, 408–419.

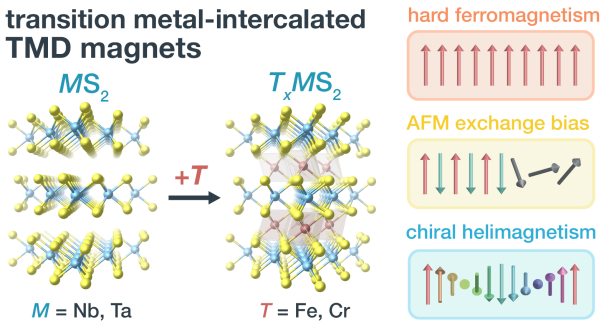
transition metal-intercalated
TMD magnets
MS_2
T_xMS_2
+T
M = Nb, Ta
T = Fe, Cr
hard ferromagnetism
AFM exchange bias
chiral helimagnetism

TOC Graphic